Laser-Induced Ultrafast Demagnetization: Femtomagnetism, a New Frontier?

Guoping Zhang[1]*, Wolfgang Hübner[1],
Eric Beaurepaire[2], and Jean-Yves Bigot[2]

[1] Max-Planck-Institut für Mikrostrukturphysik
Weinberg 2, 06120 Halle, Germany
`huebner@mpi-halle.de`
[2] Institut de Physique et Chimie des Matériaux de Strasbourg, Unité Mixte
380046, CNRS-ULP-ECPM
23, rue du Loess, 67037 Strasbourg Cedex, France
`jean-yves.bigot@ipcms.u-strasbg.fr`

Abstract. The conventional demagnetization process (spin precession, magnetic domain motion and rotation) is governed mainly by spin–lattice, magnetic dipole and Zeeman, and spin–spin interactions. It occurs on a timescale of nanoseconds. Technologically, much faster magnetization changes are always in great demand to improve data processing speed. Unfortunately, the present speed of magnetic devices is already at the limit of the conventional mechanism with little room left. Fortunately and unprecedentedly, recent experimental investigations have evidenced much faster magnetization dynamics which occurs on a femtosecond time scale: femtomagnetism. This novel spin dynamics has not been well-understood until now. This article reviews the current status of ultrafast spin dynamics and presents a perspective for future experimental and theoretical investigations.

1 Introduction

High areal density media and fast write/read heads are two basic building elements in the recording industry [1]. High density improves data rates, which require a wider electronic transport bandwidth for the reading process and a shorter reversal time for the writing process. The major obstacle lies in the writing process. As we move to data rates above 30 MB/s (nanosecond region), it is essential to understand the time dependence of the magnetization reversal processes in magnetic materials. Indeed, different timescales yield distinctive physical mechanisms, as shown in Fig. 1. On a long timescale of 100 ps–10 ns, magnetic dipole–dipole, Zeeman, and spin–lattice interactions are the major driving forces [2]. domain wall motion and rotation are modeled phenomenologically by the classical Landau–Lifshitz–Gilbert (LLG) equation [3], where electron excitations are completely ignored. On a timescale of 1 ps–100 ps (GHz), electron–phonon, phonon–phonon and, spin–lattice interactions prevail. The classical description above gradually becomes invalid

---

* Present address: Department of Physics and Astronomy, The University of Tennessee at Knoxville, TN 37996-1200, USA; `gpzhang@utk.edu`

B. Hillebrands, K. Ounadjela (Eds.): Spin Dynamics in Confined Magnetic Structures I,
Topics Appl. Phys. **83**, 245–288 (2002)

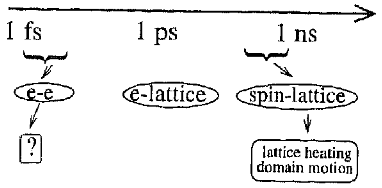

Fig. 1. Timescale for the magneto-optical recording process

as the quantum effect appears. This is an important region, where the system can recover its original magnetic moment by cooling the spin through the lattice. On a timescale from 1 fs to 1 ps, electron–electron and spin–orbit interactions dominate [4]. Electrons are heavily excited in or out of the Fermi sea [5], where the concept of electron temperature and spin temperature is not proper. In this temporal region, the classical LLG equation fails, and theoretical descriptions must be based on quantum mechanics. The focus of our study is this temporal regime where ultrafast spin dynamics occurs.

On the shortest timescale (THz), the frequency is far beyond the radiofrequency. The whole process can then be induced by optical excitation. The laser field first excites electrons; due to spin–orbit coupling, spin excitation follows this electronic excitation. Conventional magneto-optical recording also uses a laser field, but its purpose is to elevate the local temperature of the sample above the Curie or compensation temperature where the applied magnetic field rotates the magnetic moment: writing a bit. Because the procedure involves dissipative heating of the lattice, we know that the whole process is of the order of several hundred picoseconds to nanoseconds. This time has long been considered a speed limit of magneto-optical technology. However, this limit is now challenged by the present experimental observations. By using the pump-probe magneto-optical Kerr technique, *Beaurepaire* et al. [6] first reported much faster demagnetization on the timescale of a few picoseconds in a ferromagnetic Ni film. The drop of remanence, after the pump pulse, occurs on a timescale of 1–2 ps, far beyond any original expectation based on the classical picture. This observation has subsequently been confirmed by several other experimental techniques. *Hohlfeld* et al. [7] employed the time-resolved pump-probe second-harmonic generation technique and found that, even when electrons and lattice have not reached a common thermal equilibrium, the classical $M(T)$ curve can be reproduced for delay times longer than the electron thermalization time of about 280 fs. On the other hand, transient magnetization reaches its minimum at 50 fs before electron thermalization. The experiment by *Scholl* et al. [8] indicated that there might be two different mechanisms for spin relaxation taking place on two different timescales (<1 and several hundred ps). *Aeschlimann* et al. [9] found that the spin-resolved inelastic lifetime of photoexcited electrons is around 10 fs and is different for the majority and minority spins.

These new findings strongly motivated intense experimental [10] as well as theoretical [4,11,12] investigations. The latest experiment shows demagnetization during as few as 40 fs, three orders of magnitude faster than conventional demagnetization. The theory based on a many-body Hamiltonian correctly predicted this time scale [4]. In addition, it has been found that material-specific parameters, such as the exchange interaction, spin–orbit coupling, and hopping integral, play a significant role in it, and the experiment-specific parameters give us another degree of freedom to control the spin dynamics, a first step to applications. Indeed, the recent experiments demonstrate possible optical control of magnetization [10,13]. Thus, investigation along this line is going to provide us with new chances for future applications. A new frontier is emerging!

The aim of this contribution is to review the recent theoretical and experimental efforts in this field. The review is organized as follows. We shall proceed with a rapid description of the different models used to describe the magnetic properties of materials (Sect. 2). The many-body theory for ultrafast spin dynamics will be discussed (Sect. 3). In Sect. 4, the basics of laser heating of metals will be given. Then, recent results related to ultrafast spin dynamics in metals will be reviewed and discussed (Sect. 5). A summary and concluding remarks will be given in Sect. 6.

2 Historical View of Magnetization (Theory)

Magnetization is an old concept, which can be traced back to the early days of the last century. On a microscopic scale, the applied magnetic field aligns the electronic spins of a ferromagnet. A thermal field can demagnetize the sample. The temperature dependence of the magnetic moment forms the $M(T)$ curve; the Curie temperature T_C is defined as the lowest temperature with $M(T_C) = 0$. Theoretically, there are two competing models describing the magnetization process: the Heisenberg model versus the itinerant model. On a large scale, looking at the specimen as a whole, the specimen in addition consists of magnetic domains. These domains are the physical origin of hysteresis effects. The underlying dynamic process is slow and can be modeled by the classical LLG equation. Here, we ignore domains and focus only on the former two theories because we believe that the underlying mechanism of the ultrafast magnetization process is much faster than any domain propagation.

2.1 Heisenberg Model (Insulators)

A generic Hamiltonian for solids consists of the kinetic energy and the potential energy. The derivation of the Heisenberg model from the general microscopic Hamiltonian involves a number of approximations. In insulators, the electrons are well localized and virtually have no kinetic energy. This greatly simplifies the theoretical treatment because we deal only with potential energy. Magnetism originates from exchange interactions; coulombic interaction has no magnetic contribution. Thus, we are left with a pure exchange interaction term which, in second quantization, can be written as

$$H_{\text{ex}} = -\frac{1}{2}\sum_{l,l'}{}' J_{ll'} c^{\dagger}_{l\sigma} c_{l\sigma'} c^{\dagger}_{l'\sigma'} c_{l'\sigma} \,, \tag{1}$$

and

$$J_{ll'} = e^2 \int \frac{a^*(\mathbf{r}-\mathbf{r}_l)a(\mathbf{r}-\mathbf{r}_{l'})a^*(\mathbf{r}'-\mathbf{r}_{l'})a(\mathbf{r}'-\mathbf{r}_l)}{|\mathbf{r}-\mathbf{r}'|} \mathrm{d}\mathbf{r}\mathrm{d}\mathbf{r}' \,, \tag{2}$$

where $a(\mathrm{r}-\mathrm{l})$ is the Wannier function at site l. The integral $J_{ll'}$ is different from the coulombic integral by exchanging the variables $\mathbf{r}$ and $\mathbf{r}'$ in one of the Wannier functions. There is no classical analogy to this integral, which is of pure quantum nature. $c^{\dagger}(c)$ is the electron creation (annihilation) operator. If the magnet is an insulator, meaning that the particle number is a good number at every site, namely, $c^{\dagger}_{l\uparrow}c_{l\uparrow} + c^{\dagger}_{l\downarrow}c_{l\downarrow} = \text{const}$ for all l, one can derive the standard Heisenberg model rigorously for $S \geq \frac{1}{2}$,

$$H_{\text{ex}} = -\frac{1}{4}\sum_{l,l'}{}' J_{ll'}(\boldsymbol{\sigma}_l \cdot \boldsymbol{\sigma}_{l'} + 1) \,, \tag{3}$$

from (1). Here $\boldsymbol{\sigma}$ is the Pauli operator and $\sum'$ means the summation over l, l' with $l \neq l'$. If we take $\mathbf{S} = \frac{1}{2}\boldsymbol{\sigma}$, drop the constant, and assume that $J_{ll'}$ is isotropic,

$$H = -J\sum_{ll'}{}' \mathbf{S}_l \cdot \mathbf{S}_{l'} \,, \tag{4}$$

which is the standard Heisenberg model [14]. It describes the spin–spin interaction at sites l and l'. Some qualitative properties are of great interest here. If $J > 0$, the ground state is ferromagnetic; if $J < 0$, the ground state is antiferromagnetic. For the excited states, the classical picture is as follows. Suppose that due to the external perturbation (either thermally or magnetically), spin S_l at site l is deviated from its original quantized axis; through the exchange interaction, the neighboring spins experience a torque from S_l and tilt with respect to their principal axes. Simultaneously, the neighboring spins also exert a counterforce on S_l. Such interactions collectively spread out the spin motion. Now, if we view the spin motion as a whole, we can see the magnitude and direction variation of the spins just like a wave propagating from site to site: *spin-wave*. Its quantum is a magnon.

Quantitatively, a generic solution to the Heisenberg model is not possible, but we can find a simple solution for low-lying excitations. In particular, (1) for the ground state, the exact eigenvector is $|0\rangle = |S\rangle_1|S\rangle_2\cdots|S\rangle_N$, and the energy is $E_0 = -JNZS^2$, where $|S\rangle \equiv |S, m = s\rangle$ all with the same spin orientation, N is the number of sites, and Z is the coordination number. Here, we have surmised that J is positive. (2) Low-lying spin-wave excitations. In this case, one can safely ignore the higher order excitations. Through the Holstein–Primakoff transformation [15], we can find the energy spectrum as $\hbar\omega_k = 2ZJS(1-\gamma_k)$, where $\gamma_k = Z^{-1}\sum_{\delta} \mathrm{e}^{\mathrm{i}k\delta}$. Here δ is the nearest neighbor distance. (3) Temperature effect. When the temperature is taken into account, the energy spectrum is modified to $\hbar\omega_k(T) = 2Z|J|S(1-\gamma_k)\{1-\mathrm{e}(T)/S\}$, where $\mathrm{e}(T) = \frac{1}{N}\sum_{k'}(1-\gamma_{k'})\langle n_{k'}\rangle$. The magnon mode is softened now, which has been observed experimentally. Meanwhile, the magnetic moment is reduced according to the Bloch $T^{3/2}$ law: $M(T) = M(0)\{1-\alpha/S(k_{\mathrm{B}}T/2SJ)^{3/2}\}$, where $M(0) = Ng\mu_{\mathrm{B}}S$ is the zero-temperature magnetization and α is the structure factor. Note that here the reduction of the magnetization is obtained without taking into account magnon softening. Below T_{c}, it is a good approximation because magnon softening is small; however, around T_{c}, rigorously speaking, it is not valid, but due to the fact that the softenings of magnon modes at different momentum transfers are different, the side effects from the above ignorance of the mode softening are somewhat weakened.

Finally, we have two remarks before we leave this section. (i) Within the Heisenberg Hamiltonian, we do not have electrons but spins, which greatly simplifies the problem, but naturally we sacrifice some important details. In particular, this model prevents us from investigating any optical and transport properties. (ii) The temperature is the spin temperature, which is changed by the spin–lattice interaction. There is no electron temperature.

2.2 Itinerant Theory (Metals)

In ferromagnetic metals, the situation is very different; electrons are mobile and itinerant and have kinetic energies. The local electron number operator is not well-defined. Consequently, the local picture is not valid. The Heisenberg model is not applicable. One of the experimental facts contradicting the Heisenberg model is the nonintegral magnetic moment observed in ferromagnetic metals. Thus, one cannot easily reduce the many-body Hamiltonian to the pure spin Hamiltonian; instead, a fully correlated model is mandatory. The most famous one is the Hubbard model [16]. For the one-band case, the Hubbard model reads

$$H = -\sum_{ij,\sigma} t_{ij} c^{\dagger}_{i\sigma} c_{j\sigma} + U\sum_{i} n_{i\uparrow} n_{i\downarrow} \,, \tag{5}$$

where

$$\begin{aligned} t_{ij} &= \int a^*(\mathbf{r}-\mathbf{R}_i)h(r)a(\mathbf{r}-\mathbf{R}_j)\mathrm{d}\mathbf{r} \\ U &\equiv \langle ii|v|ii\rangle = e^2 \int \frac{a^*(\mathbf{r}-\mathbf{R}_i)a(\mathbf{r}-\mathbf{R}_i)a^*(\mathbf{r}'-\mathbf{R}_i)a(\mathbf{r}'-\mathbf{R}_i)}{|\mathbf{r}-\mathbf{r}'|}\mathrm{d}\mathbf{r}\mathrm{d}\mathbf{r}' \,. \end{aligned} \tag{6}$$

Here $h(r)$ is the one-particle Hamiltonian of the crystal field. U is the on-site interaction, whose physical meaning is that for two electrons of opposite spins occupying the same site, there is an energetic barrier to overcome. This term, as believed, leads to ferromagnetic ordering, though for a reasonably large U and half-filling one band, there is no rigorous result showing the existence of a ferromagnetic phase. For infinite U, $H \longrightarrow \tilde{H} = \frac{2t^2}{|U|} \sum_{ij} \boldsymbol{S}_i \cdot \boldsymbol{S}_j$ [17], and the ground state is a Néel state. It is not entirely clear how and where the magnetism comes from, exchange interaction or band degeneracies, or other, though some advances were made recently [18]. The traditional theory usually bypasses this fundamental question by assuming that the band-splitting is due to the exchange interaction. The majority and the minority spins have different band energies and consequently different occupation numbers. The uncompensated spin gives the magnetic moment.

Another way to bypass the fundamental question is to introduce the temperature, simply without specifying a mechanism for the way it comes in. We note that the temperature is the electronic temperature, not the spin temperature. In other words, there is no delay between spin and electron dynamics, though both of them are quasi-static. The Curie temperature is introduced afterwards. Under the mean-field approximation, the Hubbard model becomes the Stoner model . Note also that we include the external magnetic field h [not to confuse it with the previous Hamiltonian $h(r)$] and also the temperature,

$$\tilde{H} = \sum_{k\sigma} \tilde{E}_{k\sigma} c^{\dagger}_{k\sigma} c_{k\sigma} \,, \tag{7}$$

where $\tilde{E}_{k\sigma} = E_k - \sigma \mu_{\mathrm{B}} h + U \langle n_{\bar{\sigma}} \rangle$, and μ_{B} is the Bohr magneton. $\langle \cdots \rangle$ is the thermal average. The band splitting Δ is defined as (in the absence of the magnetic field)

$$(\tilde{E}_{k\downarrow} - \tilde{E}_{k\uparrow}) = U(\langle n_{\uparrow} \rangle - \langle n_{\downarrow} \rangle) \equiv 2\Delta \tag{8}$$

and

$$\langle n_{\sigma} \rangle = \frac{1}{N} \sum_{l} \langle n_{l\sigma} \rangle = \frac{1}{N} \sum_{k} f(\tilde{E}_{k\sigma}) \,. \tag{9}$$

Here Δ is determined self-consistently by solving (8) and (9). This also gives the magnetization $M(T)$ and the Stoner criterion for the ferromagnetic phase (FM):

$$M(T) \equiv \chi_0(T) h \,, \tag{10}$$

$$U \rho(E_F) > 1 \,, \tag{11}$$

where $\chi_0(T)$ is the magnetic susceptibility and $\rho(E_{\mathrm{F}})$ is the density of states at the Fermi level E_{F}.

Some comparisons and comments are needed here. (a) There are contrasts between the Hubbard model and Heisenberg model. In the Hubbard model, we include the kinetic energy (one-particle term) and consider only the on-site interaction, whereas in the Heisenberg model, there is only the intersite interaction. In the former, we can calculate optical and transport properties; in the latter, we cannot. In principle, within the Hubbard model, we can treat both metals and insulators, though the band gap of the latter can be very large; the Heisenberg model, however, is limited to insulators. The theoretical treatment for the Hubbard model is more formidable than that for the Heisenberg model. (b) Starting from the Hubbard model, the mean-field theory does not give a correct form for the dependence of magnetization on temperature T. For this, one has to go beyond the mean-field theory. One common way is to use the random phase approximation (RPA), where one can recover the collective behavior of spin dynamics. This yields a correct energy dispersion and consequently a correct temperature dependence. Note that in both the Stoner mean-field theory and the RPA, the temperature is the electron temperature. (c) Driving fields. In the Stoner theory, the implicit driving field is the thermal field. The thermal field elevates the system's temperature above the Curie temperature and then demagnetizes a magnet [20]. In the RPA theory, one usually employs a weak magnetic field with low frequency as the external field to perturb the system. Similar to the linear response theory, the RPA theory then calculates the linear spin–spin fluctuation around the equilibrium state. (d) Timescale. Both the Heisenberg and Hubbard models treat a static or quasi-static process, where the timescale is rarely involved. As one will see soon, in the laser field-driven demagnetization process, the timescale is of the order of a few hundred femtoseconds. It features highly nonlinear excitation, strong correlation, and a fast timescale, which require a new theoretical formalism.

2.3 Simple Theory for Spin–Lattice Relaxation: Picosecond Timescales

The characteristic *interactions* of spin relaxation processes after optical excitation on distinct timescales are (i) $\mathbf{p} \cdot \mathbf{A}$, where $\mathbf{p}$ is the crystal momentum of the electrons and $\mathbf{A}$ is the vector potential of the laser photons, (ii) electron–electron coulombic interaction leading to dynamic charge and spin fluctuations, (iii) electron–phonon interaction, and (iv) phonon–magnon interaction caused by *spin–orbit interaction* which we will approximate by static magnetocrystalline anisotropic energy. To calculate the spin–lattice relaxation time τ_{SL}, we start from the theoretical approaches successfully applied to electron spin resonance (ESR) more than three decades ago for magnetic impurities embedded in a nonmagnetic host lattice and adapt this treatment to the solid, combining phenomenological nonequilibrium thermodynamics (kinetic, theory) and microscopic equilibrium theory. Three processes (all involving phonons) contribute to spin–lattice relaxation: (a) the direct process

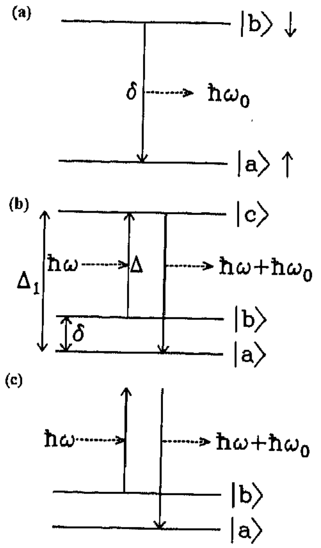

Fig. 2. (**a**) Direct process, (**b**) Orbach process, and (**c**) Raman process

(Fig. 2a,b) the Orbach process [21] (Fig. 2b), both of which are relevant only at very low temperatures; and (c) the Raman process (Fig. 2c) which we consider here: This process consists of a *spin-flip*, the *absorption* of a phonon of frequency ω, and the *emission* of a phonon of frequency $\omega + \omega_0$. The longitudinal relaxation rate T_1 in this case is independent of the magnetic field [22] and is given by

$$\frac{1}{T_1} \sim T^7 \dots T^9 , \qquad (12)$$

where T is the temperature. The Raman process is a two-phonon process of higher order which essentially uses the complete phonon spectrum. This process dominates the Orbach process (and thus also the direct process) for

$$\frac{\Delta_1}{k_B} \geq \Theta_D \qquad (13)$$

where Δ_1 is the crystal field splitting, k_B is Boltzmann's constant, and Θ_D is the Debye temperature. Nickel, for example, has

$$\frac{\Delta_1}{k_B} \approx 688\,\mathrm{K} \gg \Theta_D \approx 375\,\mathrm{K} . \qquad (14)$$

Thus, for temperatures not too low, the Raman process is dominant for the spin–lattice relaxation rate.

Therefore, in view of the experimental conditions, it appears justified to focus on *Raman*-determined spin–lattice relaxation in the solid which should be valid at intermediate lattice temperatures and picosecond timescales. The temperature range of validity forms probably the best compromise between too large temperatures where the lattice becomes unstable (above the melting point) or magnetism breaks down (above the Curie temperature) and too low temperatures where direct and Orbach processes determine the phonon-induced relaxation or the phonons become frozen. Besides, the Raman process is independent of the magnetic field.

Note that purely electronic mechanisms such as spin fluctuations in strongly correlated electronic systems mediated by nuclear spin-flips (for energy and angular momentum conservation) via hyperfine interaction require even longer timescales and are unimportant in this context because they do not involve the lattice.

As an example, to calculate the Raman-induced spin–lattice relaxation in ferromagnetic rare-earth solids, we start from the theory for spin–lattice relaxation in magnetic impurities [22]. First we consider the number of phonons ρ in the volume V and energy interval $[\delta, \delta + \mathrm{d}\delta]$

$$\rho(\delta)\mathrm{d}\delta = \frac{3V\delta^2\mathrm{d}\delta}{2\pi^2\hbar^3 v_s^3} , \qquad (15)$$

where v_s is the speed of sound in the material (e. g. Gd). The thermal occupation is given by the Bose factor,

$$\bar{p}_0(\delta) = \frac{1}{\mathrm{e}^{\frac{\delta}{k_B T}} - 1} . \qquad (16)$$

For the interaction, the usual crystal field expansion up to the second order in terms of the randomly fluctuating strains is used:

$$H_c'' \approx \varepsilon_1 \varepsilon_2 \sum_{mn} v_n^m , \qquad (17)$$

because the Raman effect is second order (see Fig. 2c). Then the transition probability from state $|b>$ to $|a>$ is given by

$$w_{b\to a} = \int \frac{2\pi}{\hbar} |< b, \bar{p}_0(\delta_1), \bar{p}_0(\delta_2) \mid H_c'' \mid a, \bar{p}_0(\delta_1) - 1, \bar{p}_0(\delta_2) + 1 >|^2 \rho(\delta_2)\rho(\delta_1)\mathrm{d}\delta_1 . \qquad (18)$$

Including the processes of stimulated emission, absorption, and spontaneous emission, the rate equation for the change of the occupation numbers of the levels $|b>$ and $|a>$ is given by (ρ_M is the mass density of the solid)

$$\dot{N}_b = -N_b w_{b\to a} + N_a w_{a\to b} = -\dot{N}_a = K[-N_b \bar{p}_0(\delta) - N_b + N_a \bar{p}_0(\delta)] . \qquad (19)$$

Using (17) and (18) leads to

$$\dot{N}_b = \frac{9\sum_{mn} |< a \mid v_n^m \mid b >|^2}{8\rho_{\mathrm{M}}^2 \pi^3 \hbar^7 v_{\mathrm{s}}^{10}} \times \int \{N_a \bar{p}_0(\delta_2)[\bar{p}_0(\delta_1) + 1] - N_b \bar{p}_0(\delta_1)[\bar{p}_0(\delta_2) + 1]\} \, \delta_1^6 \mathrm{d}\delta_1 \,. \tag{20}$$

Here, we used the fact that the square of the matrix elements of the strains ε is given by

$$\frac{\delta[\bar{p}_0(\delta) + 1]}{2Mv_{\mathrm{s}}^2} \,, \tag{21}$$

where M is the crystal mass. Using the plausible assumptions

$$\delta \ll k_{\mathrm{B}}T, \; \delta \ll \delta_1 \,, \tag{22}$$

together with the following new variables:

$$n = N_a - N_b \,,$$
$$N = N_a + N_b \,,$$

and

$$n_0 = N \tanh\left(\frac{\delta}{2k_{\mathrm{B}}T}\right) \,, \tag{23}$$

we have the kinetic equation of spin–lattice relaxation

$$\dot{n} = -\frac{1}{\tau_{\mathrm{SL,Raman}}}(n - n_0) \,. \tag{24}$$

Then, the microscopic calculation of the spin–lattice relaxation rate (which is the kinetic coefficient of the rate equation) gives the result

$$\frac{1}{\tau_{\mathrm{SL,Raman}}} = \frac{9\sum_{mn} |< a \mid v_n^m \mid b >|^2}{8\rho^2 \pi^3 \hbar^7 v_{\mathrm{s}}^{10}} \int_0^{k_{\mathrm{B}}\Theta_{\mathrm{D}}} \frac{\delta_1^6 \mathrm{e}^{\frac{\delta_1}{k_{\mathrm{B}}T}} \mathrm{d}\delta_1}{\left(\mathrm{e}^{\frac{\delta_1}{k_{\mathrm{B}}T}} - 1\right)^2} \,. \tag{25}$$

Using our previous estimate for magnetocrystalline anisotropy [23].

$$\sum_{mn} |< a \mid v_n^m \mid b >|^2 = \mid E_{\mathrm{anisotropy}} \mid^2 = \mid 735\,\mu\mathrm{eV} \mid^2 \,, \tag{26}$$

we obtain for the spin–lattice relaxation times in Gd and Ni,

$$\tau_{\mathrm{SL,Raman}}(\mathrm{Gd}) = 48\,\mathrm{ps} \,;$$
$$\tau_{\mathrm{SL,Raman}}(\mathrm{Ni}) = 304\,\mathrm{ps} \,. \tag{27}$$

Although our theoretical estimate neglects all detailed features of the electronic structure, phonon density of states, electronic correlations, effects of electronic temperature, and the detailed form of the transition matrix elements, it already yields the correct order of magnitude of τ_{SL}.

3 Theory for Ultrafast Spin Dynamics: Femtosecond Timescales

Many constraints have to be taken into account to develop a theory of ultrafast spin dynamics (USD). (1) Our model system is ferromagnetic nickel. The Hamiltonian must include the strong electron correlation. (2) The system is highly excited, which rules out any perturbative treatment in either the time dependence or the correlation part. (3) Band degeneracy should be included for 3d metals to have a correct level multiplicity and yield a ferromagnetic ground state. (4) The femtosecond timescale corresponds to interactive strength of the order of 1 eV. This means that any interaction of the same order should be included. These are our main concerns in tackling the problem of femtosecond spin dynamics.

3.1 Theoretical Formalism

We employ a free-standing Ni monolayer as an example. The Hamiltonian reads

$$H = \sum_{i,j,k,l,\sigma,\sigma',\sigma'',\sigma'''} U_{i\sigma,j\sigma',l\sigma''',k\sigma''} c_{i\sigma}^{\dagger} c_{j\sigma'}^{\dagger} c_{k\sigma''} c_{l\sigma'''} + \sum_{\nu,\sigma,K} \mathcal{E}_{\nu}(K) n_{\nu\sigma}(K) + H_{\mathrm{SO}} \tag{28}$$

where $U_{i\sigma,j\sigma',l\sigma''',k\sigma''}$ is the on-site electron interaction, which plays an important role in ferromagnetism and can be described by three parameters: coulombic repulsion U, exchange interaction J, and exchange anisotropy ΔJ. The generic values for Ni ($U_0 = 12\,\mathrm{eV}$, $J_0 = 0.99\,\mathrm{eV}$, and $(\Delta J)_0 = 0.12\,\mathrm{eV}$) are obtained by fitting the spectroscopic data, (for details see [24]). $c_{i\sigma}^{\dagger}(c_{i\sigma})$ are the usual creation (annihilation) operators in the orbital i with spin $\sigma(\sigma = \uparrow, \downarrow)$. $\mathcal{E}_{\nu}(K)$ represents the spin-independent band structure of a Ni monolayer. To obtain it, we need six parameters (for details, see [23]). $n_{\nu\sigma}(K)$ is the particle number operator of band ν in K space. H_{SO} is the spin–orbit coupling (SOC) [25]. Comparing (28) with the standard Hubbard model, one sees that the band degeneracy and spin–orbit coupling are included. A Hamiltonian of this kind is general enough to address the spin dynamics on the ultrafast time scale because it contains the necessary ingredients.

Unfortunately, it is not possible to solve it without approximation [26]. For each K point, the dimension of the two-hole basis for nickel is 66, where six orbitals per spin are taken into account, namely, five 3d orbitals and one 4s orbital. We solve the 66-state problem analytically for each atom. This solution is embedded in the crystal field given by the band structure including the translational invariance. This amounts to a crystal field theory, where the embedding is of single-electron nature. Thus it can be solved without too big numerical difficulties. Although we did not map it to the impurity problem, we believe that our treatment is similar to a K-independent self-energy correction, as performed in the dynamic mean-field theory. Once we construct the Hamiltonian within the above basis, we can diagonalize it directly.

3.1.1 Checkups

Before we go further, it is equally important to check whether our Hamiltonian can describe the essential properties of Ni. One important check is to investigate the ground-state properties, such as the magnetic moment. Ni is ferromagnetic and carries a magnetic moment. It has been well established that a prerequisite for acquiring a ferromagnetic ground state is a nonzero coulombic interaction U and exchange interaction J. We can simply check this by setting both U and J to zero. Doing so, we find that the ground state is a singlet, i. e., a paramagnetic state, which contradicts the ferromagnetic nature of Ni. Once we use the generic sets of U and J of Ni, we obtain a triplet as its ground state, from which we find a magnetic moment of the monolayer, $0.88\mu_B$ (μ_B is the Bohr magneton). This magnetic moment is larger than that in the bulk material, which is consistent with the experimental observation [27].

Moreover, we can pinpoint some basic features that show how the Coulomb and exchange interactions actually generate the ferromagnetic state. We find that for our model it is in general not true that any nonzero coulombic interaction or exchange interaction would result in a ferromagnetic phase. Actually there is a threshold which the coulombic interaction or exchange interaction has to overcome before either leads to a ferromagnetic phase. The threshold is different for U and J due to their different natures. To investigate the origin of ferromagnetism quantitatively, we first set J and ΔJ equal to zero and examine the sole effect of U while keeping the hopping integrals as they are to get a correct band structure for Ni. We find that all of the phases are ferromagnetic if U is larger than the threshold $U_c = 1.09\,\text{eV}$. We also examine how J influences the ferromagnetic phase. Analogously, we set the other interaction parameters, U and ΔJ, equal to zero. Then, it is found that the ground state of the system becomes ferromagnetic if J is larger than $J_c = 0.29\,\text{eV}$. This is a nontrivial result.

Naturally, the excited states are most challenging. From experiments, it is known that its density of states (DOS) possesses a satellite structure. This is true in our case (Fig. 3). The satellite structure at 12 eV is qualitatively consistent with Ni photoemission experiments [28]. The precise position of the satellites is, of course, given by the choice of U that, on the other hand, does not affect the timescale of spin dynamics significantly. Thus our selection of the unscreened value $U = 12\,\text{eV}$ mostly determines the satellites. It is worth noting that this satellite structure results purely from the coulombic and exchange interactions; without them, the DOS is flat on the high excitation energy side. This proves that it is necessary to include the electron correlation in ferromagnets, especially in excited states.

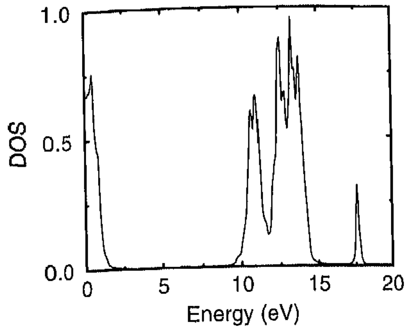

Fig. 3. Density of states for Ni thin film with a balanced band structure. Electron correlation leads to the satellite structure at the high energy side

3.1.2 Details of Ultrafast Spin Dynamics Theory

With these checkups, we begin to examine spin dynamics. Experimentally, the system is excited by laser pumping. Theoretically, we prepared the excited states according to a Gaussian distribution with width τ. At time $t = 0$, the initial state is

$$\psi(0) = \sum_{kl} p_{kl}\phi_{kl}\,, \tag{29}$$

where ϕ_{kl} is an eigenstate of momentum k and band l. The population function takes the form

$$p_{kl} = c_{kl}\mathrm{e}^{-(\omega - E_{kl})^2/\tau^2}\,, \tag{30}$$

where τ is the width of the pulse, E_{kl} is the eigenenergy of state $\{kl\}$, and c_{kl} is the normalization factor. ω is the excitation energy, through which we can change the center of the excitation profile. This mimics the experimental pump frequency. After time $t > 0$, the initial state will evolve according to the standard Schrödinger equation:

$$\mathrm{i}\hbar\frac{\partial}{\partial t}\psi = H\psi\,. \tag{31}$$

Thus,

$$\begin{aligned}\psi(t) = \mathrm{e}^{-\mathrm{i}Ht/\hbar}\psi(0) = \sum_{kl} p_{kl}\mathrm{e}^{-\mathrm{i}Ht/\hbar}\phi_{kl} &= \sum_{kl} p_{kl}\mathrm{e}^{-\mathrm{i}E_{kl}t/\hbar}\phi_{kl} \\ &\equiv \sum_{kl} p(E_{kl},t)\phi_{kl}\,.\end{aligned} \tag{32}$$

With this time-dependent state at hand, we can calculate the dynamic properties of the system.

To characterize the spin and charge dynamics clearly, we calculate both of these intrinsic quantities: $S_z(t) \equiv \langle\psi(0)|\hat{S}_z|\psi(t)\rangle$ and $N(t) \equiv \langle\psi(0)|\hat{N}|\psi(t)\rangle$, and the linear and nonlinear optical and magneto-optical susceptibilities $\chi^{(1)}_{xy}$, $\chi^{(2)}_{xzz}$ and $\chi^{(1)}_{zz}$, $\chi^{(2)}_{zzz}$. Here, $\hat{S}_z = \frac{1}{2}(\hat{n}_\uparrow - \hat{n}_\downarrow)$, $\hat{N} = (\hat{n}_\uparrow + \hat{n}_\downarrow)$, which are directly related to the observable nonlinear magneto-optical Kerr effect (NOLIMOKE) and to the second-harmonic generation (SHG) yields, respectively. Because $\chi^{(1)}_{xy}$, $\chi^{(2)}_{xzz}$, and $|\hat{S}_z(t)|$ mainly reflect the spin response and $\chi^{(1)}_{zz}$, $\chi^{(2)}_{zzz}$, and $|\hat{N}(t)|$ reflect the charge response, they will be used as indicators to evaluate spin and charge evolutions, respectively. We find that

$$\chi^{(1)}_{xy}(\omega,t) = \sum_{k,l,l'} \frac{p(E_{kl},t) - p(E_{kl'},t)}{\omega - (E_{kl} - E_{kl'}) + \mathrm{i}\eta}(\langle kl|\hat{S}_z|kl\rangle + \langle kl'|\hat{S}_z|kl'\rangle - 1) \times \langle kl|x|kl'\rangle\langle kl'|y|kl\rangle\,, \tag{33}$$

$$\chi^{(1)}_{zz}(\omega,t) = \sum_{k,l,l'} \frac{p(E_{kl},t) - p(E_{kl'},t)}{\omega - (E_{kl} - E_{kl'}) + \mathrm{i}\eta}|\langle kl|z|kl'\rangle|^2\,, \tag{34}$$

$$\begin{aligned}\chi^{(2)}_{xzz}(\omega,t) = \sum_{k,l,l',l''} & \left(\frac{p(E_{kl''},t) - p(E_{kl'},t)}{E_{kl''} - E_{kl'} - \omega + \mathrm{i}\eta} - \frac{p(E_{kl'},t) - p(E_{kl},t)}{E_{kl'} - E_{kl} - \omega + \mathrm{i}\eta}\right) \\ & /(E_{kl''} - E_{kl} - 2\omega + \mathrm{i}2\eta) \\ & \times(\langle kl|\hat{S}_z|kl\rangle + \langle kl'|\hat{S}_z|kl'\rangle + \langle kl''|\hat{S}_z|kl''\rangle - 3/2) \\ & \times\langle kl|x|kl'\rangle\langle kl'|z|kl''\rangle\langle kl''|z|kl\rangle\,,\end{aligned} \tag{35}$$

$$\begin{aligned}\chi^{(2)}_{zzz}(\omega,t) = \sum_{k,l,l',l''} & \left(\frac{p(E_{kl''},t) - p(E'_{kl},t)}{E_{kl''} - E_{kl'} - \omega + \mathrm{i}\eta} - \frac{p(E_{kl'},t) - p(E_{kl},t)}{E_{kl'} - E_{kl} - \omega + \mathrm{i}\eta}\right) \\ & /(E_{kl''} - E_{kl} - 2\omega + \mathrm{i}2\eta) \\ & \times\langle kl|z|kl'\rangle\langle kl'|z|kl''\rangle\langle kl''|z|kl\rangle\,,\end{aligned} \tag{36}$$

where $|kl\rangle$ is the eigenstate with the eigenvalue E_{kl}; η is a damping factor, $p(t) = N(t)$.

3.2 Results: Linear Optical and Magneto-Optical Responses

In the following, we monitor both charge and spin dynamics on the femtosecond timescale and investigate the influence of different intrinsic and extrinsic parameters. We start with the generic set of parameters, U_0, J_0, and $(\Delta J)_0$ for Ni. The Gaussian width W of the initial excited state is taken as broad as 20 eV to maximize the number of available channels and thus reveal the intrinsic (= fastest possible) charge and spin responses. In Fig. 4b,d $|\chi^{(1)}_{xy}(\omega,t)|$ and $|\chi^{(1)}_{zz}(\omega,t)|$ are shown, which represent the spin and charge dynamics, respectively, as measurable by typical pump-probe experiments. $\omega = 2\,\mathrm{eV}$ hereafter. The relaxation time is determined by looking at the first clear minimum [29] of $|\chi^{(1)}_{xy}(\omega,t)|$ and $|\chi^{(1)}_{zz}(\omega,t)|$. First, the figure shows that the charge and spin dynamics occur on a ten-femtosecond timescale [30], which is shorter than that observed in existing experiments. The second important result is that the spin dynamics lags behind the charge dynamics by 1 fs, which is an appreciable effect on a timescale of fs and in accordance with the recent measurement of the spin-dependent lifetime [9]. This result already shows the existence of a nonequilibrium spin memory time without involving dissipation to the lattice. We note that, at no stage of our calculation did we have to invoke the notion of either electron or spin temperature. The concept of spin temperature is particularly questionable due to the nonequilibrium and also due to the absence of well-defined quasi-particle statistics for the spins.

To pinpoint the origin of spin dynamics, we first vary the exchange interaction while the coulombic interaction $U = U_0$ is fixed. For reduced $J = J_0/10$ (Fig. 4a,c), one can see the different behavior between spin and charge dynamics more clearly. Figures 4a,b show that the exchange interaction affects the main peaks of $|\chi^{(1)}_{xy}(\omega,t)|$, and also its subsequent decay: with the de-

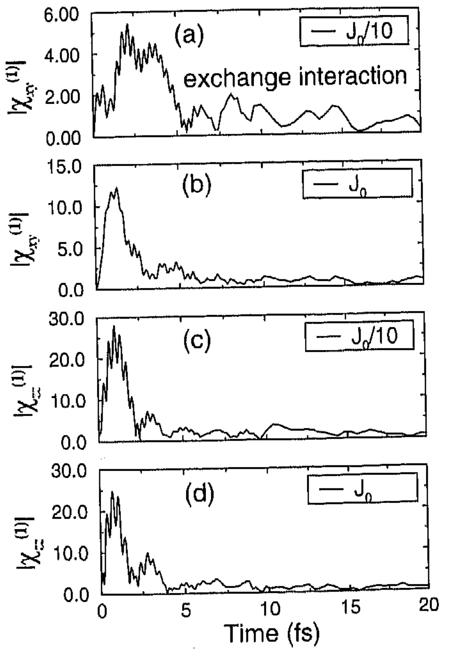

Fig. 4. Exchange interaction J effects on spin [(a) and (b)] and charge [(c) and (d)] dynamics

crease of J from J_0 to $J_0/10$, the relaxation time for spin dynamics increases from 3.4 to 5.6 fs [30], and the charge dynamics is virtually unaffected by the variation of J (see Fig. 4c,d). Thus with decreasing J, spin dynamics begins later and lags more and more behind charge dynamics.

Our calculations show that the relaxation time can be changed by tuning the exchange strength. Physically, ferromagnetism results mainly from the exchange interaction, but it has been unknown how the exchange interaction affects spin dynamics on the ultrafast timescale. Here, we clearly see that it accelerates the relaxation: because the energy scales roughly as J in the ferromagnetic system, the relaxation time scales as $1/J$. Without spin–orbit coupling (SOC), the total spin is a good quantum number, yet spin dynamics exclusively results from the loss of the quantum coherence due to dephasing of the initial excited state. The information of this dephasing is contained in $|\chi_{xy}^{(1)}(\omega,t)|$ and $|\chi_{zz}^{(1)}(\omega,t)|$, due to the temporal evolution of the complex population of the eigenstates, and dephasing occurs on different timescales for charge and spin dynamics.

When spin–orbit coupling λ is turned on to its generic value $\lambda_0 = 0.07\,\mathrm{eV}$, the spin relaxation time is determined by both λ and J. To see the effect of SOC on the relaxation process more clearly, we set $J = \Delta J = 0$ and choose $\lambda = 1.0\,\mathrm{eV}$. Comparing thick and thin lines in Fig. 5, one notices that the relaxation time decreases if λ is larger. Thus, for some noble metals or rare earths with a much larger SOC than that in Ni, optical alignment could generate ultrafast spin dynamics in two-photon photon emission (TPPE), even from nonmagnetic metals [31].

Next we study how the band structure influences spin and charge dynamics to demonstrate its material sensitivity. We change the band structure by multiplying all of the hopping integrals by a factor of 0.1. A smaller hopping integral corresponds to a more atom-like material. Figures 6a,b show spin and charge dynamics, respectively. Comparing Fig. 4b,d with the solid curves in Fig. 6a,b, one may note that upon decreasing the hopping integral from A_0 to $A_0/10$, the recurrent features in both $|\chi_{xy}^{(1)}(\omega,t)|$ and $|\chi_{zz}^{(1)}(\omega,t)|$ are more obvious and the relaxation time for spin dynamics increases up to more than 20 fs for $A_0/10$ (note the different abscissa scales). Thus, a small hopping integral as appears in nanostructured thin films, islands, clusters, or some impurities in the material slows down spin dynamics. This means that, for example, oxides [32], exhibiting both dispersive bands and nondispersive gap states, might be an ideal playground to tune the dynamic timescale at will. Besides, reducing the pulse width from 20 eV to 0.2 eV further prolongs the decay time to 100 fs (*long dashed curves* in Fig. 6a,b), which then should be easily accessible by standard experimental techniques. So, the laser width (spectral and temporal) has a very important impact on the relaxation time of spin dynamics, which deserves detailed study.

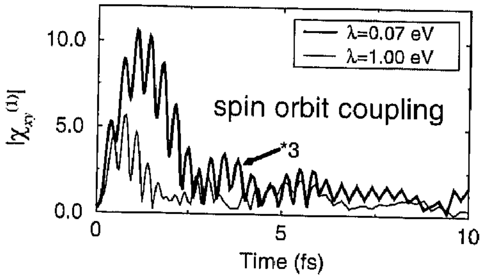

Fig. 5. Effects of spin–orbit coupling. The *thick curve*: the generic parameter for nickel; the *thin curve*: the artificially large spin–orbit coupling

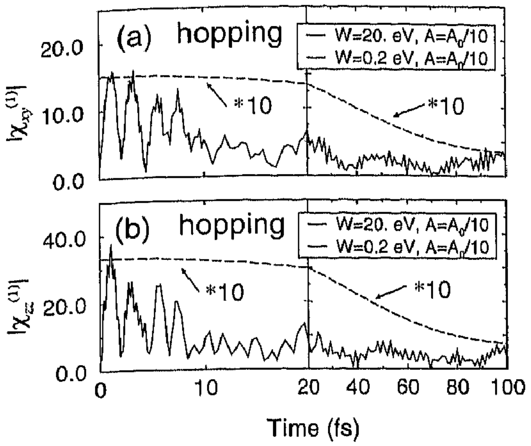

Fig. 6. Hopping integral effects on **(a)** spin and **(b)** charge dynamics. A small hopping integral corresponds to nanostructure materials

To investigate the effect of the laser spectral width (an extrinsic parameter), we choose two different widths of initial state distribution, $W = 20\,\mathrm{eV}$ (*full curves* in Fig. 7a,b) and $0.2\,\mathrm{eV}$ (*long dashed curves*), keeping the other parameters at their generic values U_0, J_0, $(\Delta J)_0$, A_0, and λ_0. With the decrease in the width, the relaxation time becomes much larger. From Fig. 7a, one may notice that for $W = 20\,\mathrm{eV}$, the decay of spin dynamics is around 3.4 fs; for $W = 0.2\,\mathrm{eV}$, it is prolonged to 14 fs. The pulse-width dependent relaxation is also obvious for charge dynamics (see Fig. 7b). For $W = 20\,\mathrm{eV}$, it decays in around 2 fs; for $W = 0.2\,\mathrm{eV}$, it lasts up to 13 fs. For real applications, the persistence of the slower decay of spin dynamics compared to charge dynamics is important because it sets the magnetic memory time. Thus, one can change extrinsic parameters to influence spin dynamics, even if one does not change material parameters.

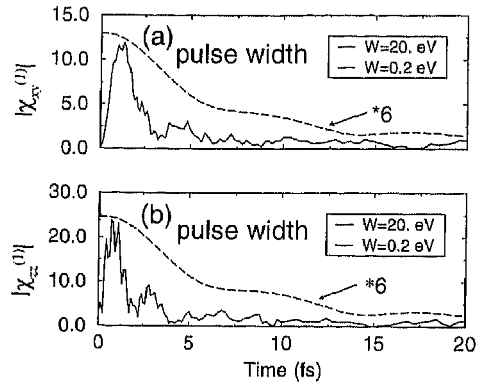

Fig. 7a,b. Effects of experiment-specific parameters. Here, we investigate the effects of laser pulse width

3.3 Results: Nonlinear Optical and Magneto-Optical Responses

We also calculated the nonlinear responses. In Fig. 8, we first show the effect of exchange coupling J on $\chi_{xzz}^{(2)}$ and $\chi_{zzz}^{(2)}$ as a function of time t. The probe frequency ω is fixed at 2 eV. The initial state is prepared at 2 eV above the ground state with a Gaussian broadening as large as 20 eV, which opens almost all of the possible decay channels. Such a large distribution width corresponds to a very large laser spectral width of a sub-femtosecond pulse. As discussed above, the purpose of this choice is to reveal the real *intrinsic* speed limit of spin dynamics in our system, which is then not delayed by experimental constraints. In Fig. 8a,b, the generic parameters of Ni monolayers are used. There are several interesting features that should be mentioned. One notices that in Fig. 8a, $\chi_{xzz}^{(2)}$ first comes up very quickly and reaches its maximum at about 2–3 fs. Then, $\chi_{xzz}^{(2)}$ undergoes a sharply decreasing envelope and oscillates with a very short period. The dynamics of $\chi_{xzz}^{(2)}$ settles down at around 10 fs (decay to 1/e of maximum), which indicates complete dephasing. As mentioned before, $\chi_{xzz}^{(2)}$ is related to the spin response. Thus, we estimate that the spin relaxation time is about 10 fs, which is consistent with our previous results for time-resolved linear magneto-optics and optics based on $\chi_{xy}^{(1)}$ and $\chi_{zz}^{(1)}$. For charge dynamics, we see a different scenario. In Fig. 8b, $\chi_{zzz}^{(2)}$ is plotted as a function of time t. One sees that the rise time of $\chi_{xzz}^{(2)}$ is similar to that of $\chi_{xzz}^{(2)}$, but its decay time is shorter. After 5 fs, the value of $\chi_{zzz}^{(2)}$ is already close to equilibrium. This means that charge dephasing is faster than spin dynamics. If one compares Fig. 8a with 8b, one sees a clear difference between spin and charge dynamics. Basically spin dynamics lasts about twice as long as charge dynamics. This has an important consequence because it demonstrates the spin memory effect: though charge dynamics finishes, spin dynamics is still alive, which is crucial for future applications.

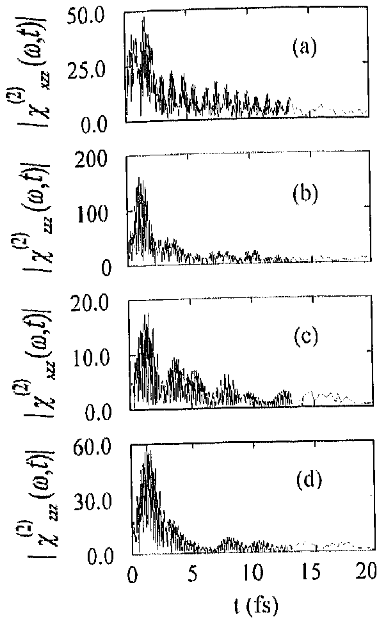

Fig. 8. Effects of exchange interaction integrals on nonlinear magneto-optical and optical responses. (**a**) and (**b**) are for the generic J_0 for nickel; (**c**) and (**d**) are for the reduced $J = J_0/10$

The main difference in the time-resolved nonlinear response compared to the linear response, which is particularly evident for magnetic dynamics, consists of an additional "bunching" of the structures resulting from the simultaneous presence of ω and 2ω resonances in (35) and (36).

To get a handle on the microscopic origin of the observed magnetic dynamics, let us try to investigate the effect of the on-site exchange coupling J by reducing J to $J_0/10$. The corresponding time dependences of $\chi_{xzz}^{(2)}$ and $\chi_{zzz}^{(2)}$ are shown in Fig. 8c,d, respectively. It can be seen that $\chi_{xzz}^{(2)}$ first comes up within 2 fs. After that, a recurrence appears with a rather large amplitude. Compared with Fig. 8a, $\chi_{xzz}^{(2)}$ oscillates with a longer "bunching" period, and the loss of coherence is weaker. We estimate that the relaxation time is about 10 fs, but the period is nearly twice as long as that in Fig. 8a. This demonstrates that the decrease of exchange interaction prolongs the period of oscillations. For charge dynamics, the change is relatively small when we reduce J from J_0 to $J_0/10$. This can be seen from Fig. 8d where we plot $\chi_{zzz}^{(2)}$ as a function of time t. Comparing Fig. 8b,d, one finds that the overall variation of $\chi_{zzz}^{(2)}$ with time is nearly identical. This is understandable because the exchange interaction acts more directly on the spin degree of freedom by changing the spin dependence of the electronic many-body states microscopically. Consequently, spin dynamics will be affected more strongly than charge dynamics. However, even electrons with different spin orientations play a similar role in charge dynamics. Thus, charge dynamics is basically independent of the spin state. That is why the exchange interaction does not affect charge dynamics significantly.

Finally, as our previous studies already showed [4,12] for linear pump-probe calculations, band structure will also influence the relaxation process. Its effect is actually very significant. Our results on $\chi^{(1)}_{xy}$ and $\chi^{(1)}_{zz}$ already showed that hopping integrals can modify the relaxation process strongly. Analogously, this will be reflected in nonlinear optical responses $\chi^{(2)}_{xzz}$ and $\chi^{(2)}_{zzz}$. To investigate the effect of band structure, we reduce the hopping integrals to one-tenth of the original nickel hopping integrals and keep the rest of the parameters unchanged. Here, the initial excited state is also prepared 2 eV above the ground state with a Gaussian broadening of 20 eV. The results are shown in Fig. 9. One finds that the change in both $\chi^{(2)}_{xzz}$ and $\chi^{(2)}_{zzz}$ with time is very different from the previous results. From Fig. 9a, one notices that $\chi^{(2)}_{xzz}$ increases sharply within 5 fs. The strong oscillation lasts about 20 fs, where no clear decay can be seen. The outline of $\chi^{(2)}_{xzz}$ ranging from 0 fs to 20 fs forms a broad peak. After 20 fs, dephasing occurs, but the envelope of $\chi^{(2)}_{xzz}$ decays only slowly. Comparing Fig. 8a,b with Fig. 9a,b, respectively, one sees that the reduction of the hopping integrals slows down both spin and charge dynamics considerably. The envelope of $\chi^{(2)}_{xzz}$ now decays on a timescale of 30–40 fs. The appreciably fast oscillation in the long-time tail survives beyond 80 fs.

3.4 Results: Intrinsic versus Extrinsic

Quite often, the extrinsic constraints imposed by experimental techniques may blur the intrinsic physical process. To gain some insights into it, in Fig. 10, we perform a detailed comparison between those experimental observables and intrinsic quantities [i.e., $|\hat{S}_z(t)|$ and $|\hat{N}(t)|$]. Now, the initial excited state is prepared 2 eV above the ground state with a Gaussian broadening of only 0.2 eV, which simulates a narrow laser spectral width, in contrast to the previously used width of 20 eV. This allows us to see the effect of the laser spectral width clearly. The same Ni parameters are used. In Fig. 10a,b, we show the results up to 40 fs. The abscissa and ordinate in Fig. 10a,b denote the real and imaginary parts of intrinsic spin and charge dynamics, $S_z(t)$ and $N(t)$, respectively. Note that these quantities cannot directly be observed experimentally and are only theoretically accessible. The arrows refer to the temporal direction, and the centers are the final positions of $S_z(t)$ and $N(t)$. One notices that spin dynamics needs about six cycles to reach nearly its final value, whereas for charge dynamics only three cycles are needed. This demonstrates again that spin dynamics is delayed with respect to charge dynamics. We find that comparing these intrinsic quantities, one can see a clear

---

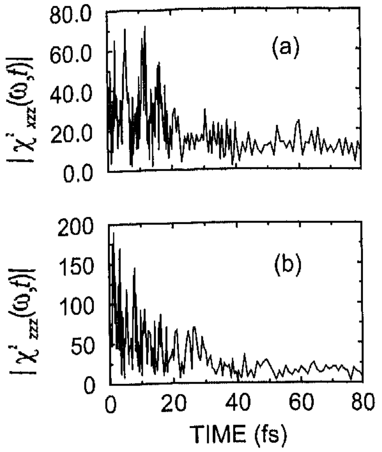

Fig. 9. Effects of the hopping integral on nonlinear magneto-optical and optical responses. A prolongation of both (a) spin and (b) charge dynamics is also realized with reduced hopping

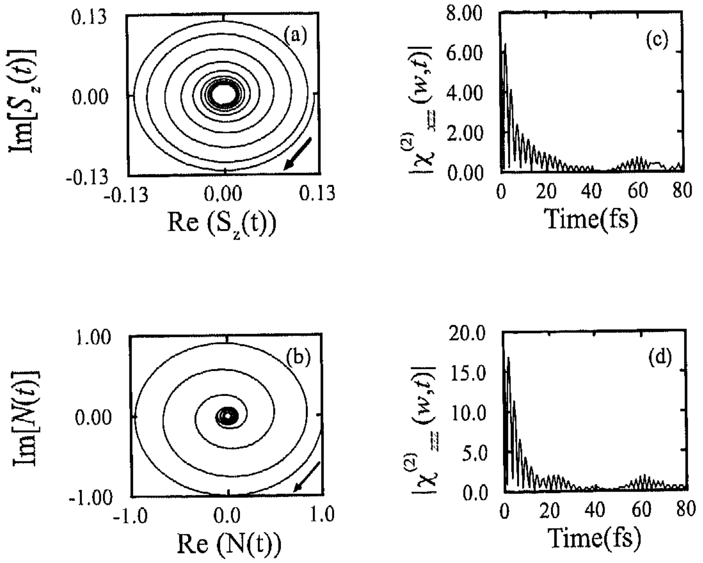

Fig. 10. A comparison of the intrinsic (a) spin and (b) charge dynamics with the (c) magneto-optical and (d) optical responses

difference between spin and charge responses, which is not blurred by the details of the experimental conditions. However, strictly speaking, there can be no complete one-to-one correspondence between $S_z(t)$ and $|\chi^{(2)}_{xzz}(\omega,t)|$ or $N(t)$ and $|\chi^{(2)}_{zzz}(\omega,t)|$ because the experimental observations also reflect the real response to the external probe-laser field.

3.5 Our Explanations: Spin and Charge Dephasing

As we have seen repeatedly, there is a clear delay between spin and charge dynamics. To understand this, we invoke a simple picture to explain this difference. In Fig. 11, we show the complex population (32) of the excited states versus the eigenenergy. At time $T = 0$, all of the states are in phase, (see the vertical arrows). After time $T > 0$, the phases of these states will change according to their explicit energies (see the tilted arrows). The phase changes are different for different eigenvalues. Thus, these states begin to run out of phase against each other, and dephasing occurs. For charge dynamics, all of the excited states contribute to dephasing. This means that dephasing is strongest. However, in spin dynamics, not all of the states are relevant; only those states (triplets) with magnetic moments (see the states with double arrows) can contribute. The number of decay channels in spin dynamics is much smaller than that in charge dynamics, which leads to slower decay of spin dynamics. Hence, spin dynamics proceeds much longer than charge dynamics. This explains why spin dynamics always delays with respect to charge dynamics.

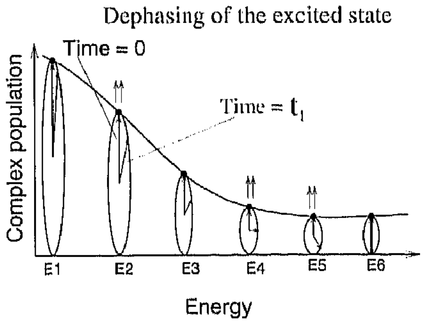

Fig. 11. The time-dependent complex population versus eigenenergies

4 Nonequilibrium Heating in Metals

In this section, we discuss the relaxation processes following the absorption of an ultrashort laser pulse in a metal.

4.1 Heating Metals with Ultrashort Laser Pulses

Four steps are usually considered in laser heating of metals, and they may in some circumstances overlap in time [33,34,35,36,37,38,39,40,41,42]: (1) the photon energy is deposited within the skin depth of the metal (≈ 20 nm) exciting electron–hole pairs (quasi-particles), (2) electron–electron interaction leads to thermalization of the quasi-particles, (3) energy is exchanged between quasi-particles and phonons, and (4) energy propagates in the medium. The absorption of energy occurs via intra- and interband optical transitions. Then, the energy distribution of the excited states changes in time due to electron–electron scattering, until it reaches a Fermi–Dirac distribution. This process is characterized by a thermalization time τ_th after which the electrons have a well-defined high temperature. The energy then relaxes from the electrons to the lattice due to the electron–phonon interaction with a characteristic relaxation time τ_el. The next step involves heat propagation. Energy is then dissipated in the environment. In the context of this review, this propagation effect, which can be described by the Fourier equation and which occurs in the nanosecond timescale, will be ignored. Historically, athermal electron distribution was first neglected. The problem was formulated in the so-called two-temperature model [42] and was solved to compare the rates of thermoionic and thermoelectric emission from laser exposed surfaces [43]. In this model, the rate equations for electron and lattice temperatures (resp. T_e and T_l) are given by

$$C_\mathrm{e}(T_\mathrm{e})\frac{\mathrm{d}T_\mathrm{e}}{\mathrm{d}t} = -G_\mathrm{el}\,(T_\mathrm{e} - T_\mathrm{l}) + P(t)\,, \tag{37a}$$

$$C_\mathrm{l}(T_\mathrm{l})\frac{\mathrm{d}T_\mathrm{l}}{\mathrm{d}t} = G_\mathrm{el}(T_\mathrm{e} - T_\mathrm{l})\,, \tag{37b}$$

where C_e and C_l are the electronic and lattice specific heats, G_el the electron–phonon coupling constant, and P the laser power density absorbed in the material. Because we address thin films, heat conduction has been neglected in (37) and (38). Laser power density enters only in (37a) because energy is deposited initially in the electron system. G_el is related to the microscopic parameters of the electron–phonon interaction [44,45]; typical values for metals are 10^{16}–$10^{17}\,\mathrm{Wm^{-3}K^{-1}}$. Measurements of G_el from ultrafast spectroscopy provide valuable information about the electron–phonon coupling strength [36]. In the perturbative limit, i.e., for a weak temperature elevation $[T_\mathrm{e}(t) - T_\mathrm{l}(t) \ll T_\mathrm{l}(t)]$, the specific heat coefficients are constant and (37a) and (37b) become linear: T_e decays exponentially with a characteristic time $\tau_\mathrm{el} = C_\mathrm{e}/G_\mathrm{el} \sim 1\,\mathrm{ps}$. A more detailed approach consists of taking into account the athermal electron population created by the absorption of the pump pulse. Now, the relevant dynamic quantity is the number of excited particles $n(\epsilon,t)$. The time dependence of n is divided into contributions arising from electron–electron and electron–phonon scattering. The computation of n from such a model of rate equations requires knowledge of the electron and the phonon spectra together with a many-body description of the quasi-particle interactions. Dynamic processes have been considered in some detail only for noble metals [45,46]. It is known from Fermi liquid theory that in bulk materials, hot electrons (holes) with an excitation energy ϵ have a lifetime $\tau_0(\epsilon_F^2/\epsilon^2)$ [47]. For gold, typically $\tau_0 = 0.6\,\mathrm{fs}$, so that the lifetime of photoexcited electron–hole pairs is in the femtosecond range. However, the average value $\langle\tau_{ee}\rangle = \tau_0(\epsilon_F^2/\langle\epsilon^2\rangle)$ that has the physical meaning of the thermalization time τ_{th}, amounts rather to 100 fs. When an energy-resolved description of the athermal electron population is not necessary, a phenomenological description can be used. The electronic distribution is separated into a thermalized part, characterized by its temperature T_e, and an athermal contribution characterized by a parameter N, representing the energy density per volume of the nonthermal electrons. Then, three coupled differential equations are necessary [40]:

$$\frac{\mathrm{d}N}{\mathrm{d}t} = -\alpha N - \beta N\,, \tag{38a}$$

$$C_e(T_e)\frac{\mathrm{d}T_e}{\mathrm{d}t} = -G_{el}\,(T_e - T_l) + \alpha N\,, \tag{38b}$$

$$C_l(T_l)\frac{\mathrm{d}T_l}{\mathrm{d}t} = G_{el}(T_e - T_l) + \beta N\,. \tag{38c}$$

The parameter α and β describe the heating rate of the thermalized electrons and phonons from the nonthermal electrons, respectively. Here $\alpha = 1/\tau_{th}$. Experimentally, the electronic dynamics of electron in metals is determined by measuring the transient reflectivity and transmittivity of a thin film. The time dependence of the optical indexes can be obtained from such data [48]. To accurately describe the dynamics of the optical response of a metallic film, one has to consider (38) together with a model for the medium dielectric function. Two contributions have to be considered, associated with intraband and interband optical transitions. The intraband term is usually taken into account by a Drude-like dielectric function. The interband term involves mostly transitions from the d bands to the conduction states. The occupation of these states depends on the temperature $T_e(t)$.

4.2 Three-Temperature Model of Ferromagnets

Because the specific heat of ferromagnetic metals is usually split into electronic, magnetic, and lattice contributions [49], a first approach to modeling ultrafast spin dynamics is to extend the two-temperature model by adding an equation related to the spin subsystem:

$$C_e(T_e)\frac{\mathrm{d}T_e}{\mathrm{d}t} = -G_{el}\,(T_e - T_l) - G_{es}\,(T_e - T_s) + P(t)\,, \tag{39a}$$

$$C_l(T_l)\frac{\mathrm{d}T_l}{\mathrm{d}t} = G_{el}(T_e - T_l) - G_{sl}\,(T_l - T_s)\,, \tag{39b}$$

$$C_s(T_s)\frac{\mathrm{d}T_s}{\mathrm{d}t} = G_{es}(T_e - T_s) - G_{sl}\,(T_l - T_s)\,. \tag{39c}$$

It is straightforward to add an additional equation to (38), in the same spirit as in (38), to take into account the nascent non-equilibrium electron population [50]. Figure 12 shows a numerical solution, applied to a nickel film, using a predictor corrector Adam method. The laser source term is a Gaussian pulse of 100-fs duration. The lattice specific heat was $C_l = 2 \times 10^6\,\mathrm{Jm^{-3}K^{-1}}$. Because of the strong variation of the density of states of Ni around the Fermi level, it is necessary to go beyond the usual linear variation of the electronic specific heat with T_e. The electronic specific heat has been computed from the theoretical density of states of ferromagnetic nickel. The spin specific heat C_s, which has a pronounced peak at the Curie temperature $T_c = 631\,\mathrm{K}$, is deduced from the temperature-dependent total specific heat by subtracting the contributions due to C_e and C_l. The coupling constants $G_{ij}(i,j = \mathrm{e,l,s})$ are respectively: $G_{el} = 8 \times 10^{17}\,\mathrm{Wm^{-3}K^{-1}}$, $G_{es} = 6 \times 10^{17}\,\mathrm{Wm^{-3}K^{-1}}$, $G_{sl} = 0.3 \times 10^{17}\,\mathrm{Wm^{-3}K^{-1}}$. Similar values of G_{el} have been observed for metals [36,37]. G_{es} and G_{sl} are two free parameters which have been adjusted to reproduce the observed dynamics that we will describe in Sect. 5. The temporal behavior in Fig. 12a shows that initially the energy is deposited in the electron subsystem, leading to a maximum of T_e (650 K) which is reached just after excitation. The increase in spin temperature T_s is delayed with respect to T_e. It reaches its maximum value (580 K) in ~ 1 ps. Simultaneously, energy is transferred from the electrons and spins to the lattice and T_e, T_s and T_l slowly reach the equilibrium temperature 540 K in a few picoseconds. When the initial non-thermal electron distribution is taken into account via a rate equation similar to (refatherma), the dynamics is different only within the first few hundreds of femtoseconds. In Fig. 12b, the corresponding simulation is represented using the parameter value $1/\alpha = 70\,\mathrm{fs}$. The inset represents the temporal evolution of the nonequilibrium population $N(t)$ which is delayed compared to the pulse excitation $P(t)$. Comparison of Figs 12b,c shows that the dynamics computed with the actual density of states of Ni is mimicked by using the linear expansion $C_e = \gamma T_e$ with $\gamma = 6 \times 10^3\,\mathrm{Jm^3\,K^{-2}}$, a value much larger than that directly measured from calorimetric experiments at low temperature [6,49,50]. This difference is therefore explained by the variation in electronic density of states around the Fermi level of Ni.

The model above raises two important questions. First, is it legitimate to describe dynamics with three different temperatures? Second, what is the

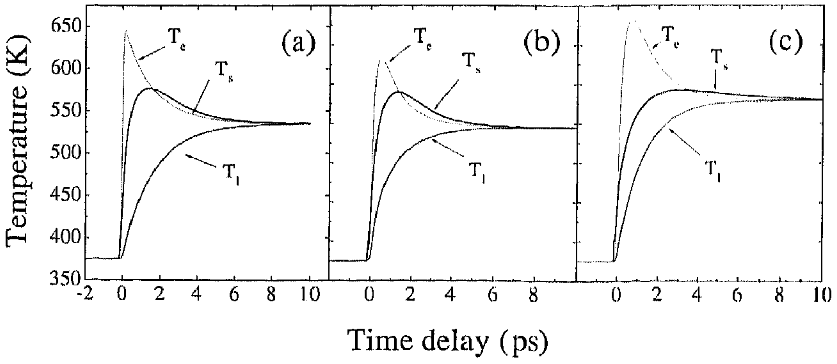

Fig. 12. Simulated temperature profile for a Ni film excited by an ultrashort laser pulse. (a) (39) have been solved numerically with the parameters reported in the text. (b) Same as in (a) but nonthermal electron population, with a lifetime 70 fs, is taken into account. (c) Same as in (b) with electronic heat capacity computed from the theoretical density of states

physical meaning of the electron–spin and spin–lattice coupling constants G_{es} and G_{sl}? These two questions are at the center of the recent observations on ferromagnetic films which we will describe extensively in Sect. 5. There is presently no satisfying microscopic theory that accounts for the observed spin dynamics induced by femtosecond optical pulses. Our current understanding of the situation, based on experimental results, is the following: (1) energy is initially deposited only in the electron subsystem because spins are conserved in the transitions under dipole approximations; (2) magnetization is strongly modified on a timescale when the lattice temperature has not yet changed significantly. These two facts plead in favor of a mechanism that transfers energy efficiently from electrons to spins, without any major contribution from the lattice. The corresponding coupling G_{es} may then correspond to the spin–orbit interaction. However, one should not exclude spin-flip processes occurring in the interacting electron gas. Such processes may be assisted by scattering between the observed d electrons and the unobserved conduction electrons leading to a change in the majority ($N_{d\uparrow}$) and minority ($N_{d\downarrow}$) spin populations and therefore to the magnetization $M_d \sim (N_{d\uparrow} - N_{d\downarrow})$. In this case, there is a priori no reason for the electron and spin temperatures to follow the same dynamics. The mechanism that is generally considered for the coupling G_{sl} between the spins and the lattice, is the interaction between phonons and spin-waves. It is important to stress that the concept of spin-waves may not apply in the ultrafast dynamic regime. Indeed, for short temporal delays, low-frequency magnons are not involved. Therefore, the rate of energy transfer between the spin subsystem and the lattice may be different depending on the conditions of excitation. When using nanosecond or subnanosecond optical pulses [2], the slow increase in the lattice temperature induces a corresponding change in magnetization with a time constant τ_m.

The microscopic mechanism is the coupling of the spins to the anisotropic fluctuations in the crystal field produced by phonons. This coupling is mediated by spin–orbit interaction, as discussed in Sect. 2.3. The microscopic calculation shows that τ_m scales with the magnetocrystalline anisotropic energy. Typical values are $\tau_m = 48\,\mathrm{ps}$ for Gd and 310 ps for Ni, in agreement with experimental results [2,51]. These values are also compatible with the 45-ps spin–lattice relaxation time in gold [52]. Except for materials with very large magnetocrystalline anisotropy, this mechanism is not expected to play an important role in the ultrafast regime described in this review. Note that the anisotropic fluctuations in magnetization correspond to the damping mechanism which appears in the phenomenological models of Landau–Lifschitz and Gilbert mentioned in the introduction.

5 Ultrafast Spin Dynamics: Experimental Review

Linear and nonlinear magneto-optical (MO) techniques are described in separate chapters of this book. Only some basic elements will be given here.

5.1 Magneto-Optical Response

As previously, nonlinearities are defined from the expansion of the electric polarization as a function of the exciting electric fields

$$P_i = \chi_{ij} E_j(\omega) + \chi_{ijk} E_j(\omega) E_k(\omega) + \cdots \,. \tag{40}$$

The linear (χ_{ij}) and nonlinear (χ_{ijk} and higher order) susceptibility tensor elements are then expanded as a function of the magnetization (a first-order approximation is usually sufficient).

5.1.1 Linear Magneto-Optics

In the presence of a uniform magnetic field in the z direction, the susceptibility tensor of an isotropic medium acquires nondiagonal elements. As a consequence, the linear magneto-optical effects (Faraday effect in transmission geometry or Kerr effect in reflection geometry) manifest by the modification of the polarization state of a probe beam after its interaction with a magnetized sample. From an experimental point of view, the Faraday and polar Kerr effects result from the application of a magnetic field perpendicular to the plane of the film. They usually produce larger effects than the longitudinal Kerr effect which is obtained with a magnetic field that lies in both the plane of incidence and in the plane of the film. The simplest description of the MO effects is the classical Voigt model [53] that allows correlating the optical and magneto-optical quantities (Kerr and Faraday angles) with the optical and magnetic properties of a film. The Kerr rotation and ellipticity are given by

$$\Phi_K = \theta_K + i\varepsilon_K = \frac{-\chi_{xy}}{\chi_{xx}\sqrt{1+4\pi\chi_{xx}}} \,. \tag{41}$$

The measurement of these quantities allows us to determine the nondiagonal part of the susceptibility tensor. The ratio between the diagonal and non-diagonal elements of the susceptibility tensor is typically of the order of 10^{-2}, so that Kerr rotations in metals do not exceed 1° for wavelengths ranging from the near ultraviolet (UV) to the near infrared (IR). In the original Voigt model, χ_{xx} is related to the optical indexes of the material and χ_{xy} in addition to the magnetic induction B_0 acting on the electrons. The corresponding B_0 is typically 10^3 T, and its origin is the Weiss molecular field, rather than an applied magnetic field. However, in the visible and UV parts of the spectrum, light absorption occurs via interband transitions that are not explicitly taken into account in this description. The calculation of the Kerr or Faraday rotation requires a microscopic model of the susceptibility tensor. In metals, it is a difficult task because one has to take into account the strong correlation between the electrons and the coupling of the optical and magnetic fields with charges and spins.

Ab initio calculations of the dielectric tensor have been performed for ferromagnetic 3d metals for wavelengths from the IR to the UV region [54]. Good agreement with the experiments has been obtained. The important result is that interband transitions dominate the magneto-optical response in the visible part of the optical spectrum. It was shown that Kerr rotations are approximately proportional to both the spin–orbit and exchange interaction, substantiating the relationship between MO quantities and magnetization.

The theory above applies to the magneto-optical response of a ferromagnetic material excited by a plane wave. In the dynamic case, ideally, one would have to consider the time-dependent interactions among the excited electrons. This difficult task can be reduced in a first approximation to a simpler one by considering a time-dependent electron temperature using, for instance, the two-temperature model of Sect. 4.1. The time-dependent magnetization then depends on the dynamics of the electronic population distributed apart from the Fermi level. This approach is valid, however, only when the electrons are thermalized, and therefore it does not allow describing spin dynamics in the initial time period. It also does not take into account the dynamic aspect of the coupling between the electron and spin systems which was introduced qualitatively in Sect. 4.2 by a three-temperature model.

5.1.2 Nonlinear Magneto-Optics

Magnetic second-harmonic generation (M-SHG) is a recent tool which allows studying magnetic properties of surfaces [55] and buried interfaces [56]. The specificity of this method is due to the noncentrosymmetry of the interfaces, which is at the origin of SHG. Because nonlinear optical effects require large peak power and short pulses, they are a priori compatible with pump and probe measurements of ultrafast dynamics.

The second order nonlinear polarization is given by

$$P_i\left(2\omega\right) = \chi^{(2)}_{ijk}\left(M\right) E_j\left(\omega\right) E_k\left(\omega\right) ,$$

where $\chi^{(2)}$ can be split into even ($\chi^{(2)}_{\text{even}}$) and odd ($\chi^{(2)}_{\text{odd}}$) contributions with respect to the magnetization. To the lowest order in the magnetization, $\chi^{(2)}_{\text{even}}$ is considered independent of the magnetization and $\chi^{(2)}_{\text{odd}}$ proportional to the magnetization. Denoting by ϕ the phase difference between the complex quantities $\chi^{(2)}_{\text{even}}$ and $\chi^{(2)}_{\text{odd}}$ and disregarding Fresnel factors that take into account the actual experimental geometry, the second-harmonic intensity $I(2\omega)$ is given by:

$$I\left(2\omega, \pm M\right) \propto I^2\left(\omega\right) \left[\left|\chi^{(2)}_{\text{even}}\right|^2 + \left|\chi^{(2)}_{\text{odd}}\left(M\right)\right|^2 \pm 2\left|\chi^{(2)}_{\text{even}}\right|\left|\chi^{(2)}_{\text{odd}}\left(M\right)\right|\cos\phi\right] \quad (42)$$

This expression shows that $I(2\omega)$ provides direct magnetic information. Despite very low efficiency [typically, $I(2\omega)/I(\omega) \sim 10^{-12}$ even for peak power of $\sim 10^{12}\,\mathrm{Wm^{-2}}$), M-SHG provides detailed surface/interface sensitive magnetic information. It was also shown experimentally [57] and theoretically [58] that nonlinear MO effects give rise to nonlinear Kerr rotations that can be two orders of magnitude larger than linear Kerr rotation. Recent significant experiments related, for example, to surface magnetism, quantum-well states and imaging of surface domains can be found in [55,56,59].

5.2 Experimental Apparatus

In this section, we present different techniques that allow us to determine time-dependent magnetization. In particular, we describe in detail the apparatus that has been used by the authors to perform the time-resolved magneto-optical measurements reported in Sect. 5.3.

5.2.1 Time-Resolved Magneto-Optical Measurements

Time-resolved MO measurements were made using a femtosecond laser system and a static magnetic field. The femtosecond pulses are produced by a tunable titanium:sapphire laser. The pulses issued from an oscillator operating at 80 MHz are amplified in a regenerative amplifier pumped by a Nd:YLF (yttrium lithium fluoride) laser with a repetition rate of 5 kHz. The maximum energy per pulse is ~ 200 µJ tunable in the range 760–860 nm, and the pulse duration is ~ 100 fs. Part of the amplified beam can be frequency doubled (380–430 nm) in a 1-mm thick BBO crystal to make frequency nondegenerate pump-probe measurements. The intensity ratio of the pump and probe beams is 20:1 and their spot diameters focused on the samples are, respectively, ~ 100 µm and ~ 50 µm. The overlap of the two beams is monitored with a CCD camera. Figure 13 shows the laser setup and the experimental configuration. Early experiments on nickel films were done with a different laser system. In that case the femtosecond pulses were produced by a colliding-pulse mode-locked cavity operating at 620 nm and amplified at 5 kHz with a

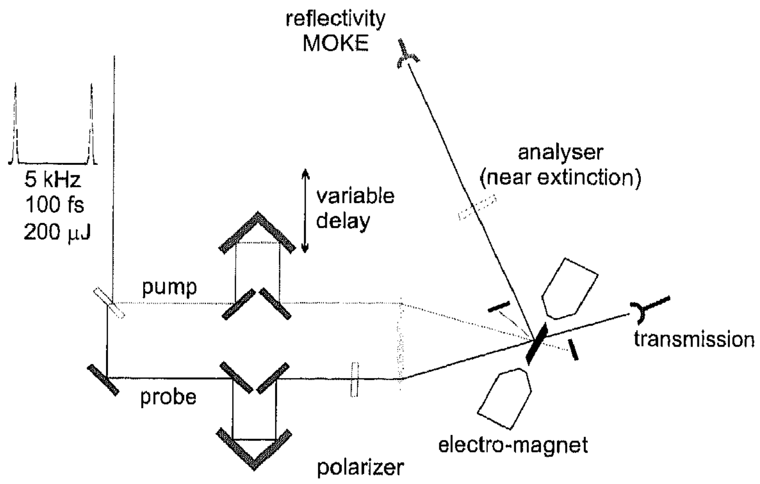

Fig. 13. Typical setup used for time-resolved optical and magneto-optical measurements

copper vapor laser. The duration of the amplified pulses is 80 fs and the maximum pulse energy is 10 μJ, with a central wavelength at 620 nm. Different types of measurements can be made on both laser setups.

i) When measuring electron dynamics, no magnetic field is applied. The differential transmission of a thin film $\Delta T/T(t) = (T_{\mathrm{on}} - T_{\mathrm{off}})/T_{\mathrm{off}}$ is measured as a function of the temporal delay t between the pump and probe; $T_{\mathrm{on}}(T_{\mathrm{off}})$ is the normalized probe transmission with (without) the pump. Similarly, the differential reflection $\Delta R/R(t)$ is measured simultaneously. The detection scheme is a synchronous detection using a chopper and a lock-in amplifier. The simultaneous measurement of the differential transmission and reflection as a function of the pump-probe delay allows to retrieve the time-dependent complex dielectric function $\varepsilon(t)$ of the metal. We denote by $\Delta\varepsilon_1$ and $\Delta\varepsilon_2$ the corresponding changes of the real and imaginary parts of $\varepsilon(t)$, induced by the pump pulse. They are the physical quantities of interest in understanding electron dynamics. The dielectric function is retrieved following the procedure used by *Rosei* [48] to analyze static thermomodulation measurements. In this procedure, the Fabry–Pérot-like transmission T and reflection R of a thin metallic film of thickness ℓ are functions of the refractive index n, the wavelength λ, and the film thickness ℓ. They can be differentiated with respect to a small variation in the refractive index $\Delta n = \Delta n_1 + \mathrm{i}\Delta n_2$ to give

$$(BC - AD)\,\Delta\varepsilon_1 = B\,(\Delta T/T) - D\,(\Delta R/R)\,, \tag{43a}$$

$$(BC - AD)\,\Delta\varepsilon_2 = C\,(\Delta R/R) - A\,(\Delta T/T)\,, \tag{43b}$$

where A, B, C and D depend on n, λ and ℓ and the dielectric function is obtained from $\varepsilon = \varepsilon_1 - \mathrm{i}\varepsilon_2 = n^2$. This procedure requires that the material parameters are known. In particular, the thickness of the film, as well as its linear complex refractive index, has to be determined accurately. In our experiments, they are determined by a combination of X-ray diffraction at grazing incidence and by ellipsometric measurements. In static thermomodulation experiments, where the temperature of the lattice Θ_{l} is increased via a current applied to the sample, relations (43) correspond to a spectral variation of the dielectric function $\Delta\varepsilon_1(\omega)$ and $\Delta\varepsilon_2(\omega)$. Here, they correspond to a temporal variation $\Delta\varepsilon_1(t)$ and $\Delta\varepsilon_2(t)$. In this case, the change in the dielectric function comes from a modification of the electronic distribution induced by the laser pulse, or equivalently, induced by a change in the electronic temperature $\Delta\Theta_{\mathrm{e}} = \Theta_{\mathrm{e}}(t) - \Theta_{\mathrm{e}}(-\infty)$, when the electrons are in a well-defined thermal distribution.

ii) When measuring the dynamics, an electromagnet allows one to vary the static magnetic field H in the range ±3 kOe (±240 $\mathrm{Am^{-1}}$), which is set parallel to the plane of the sample. The polarization of the pump and probe beams are s, p, or σ^+, and they can be varied independently. As sketched in Fig. 13, the magneto-optical signal is obtained by analyzing the probe beam at an angle of $90^\circ + \theta_\varepsilon$ with respect to its incident polarization direction; θ_ε is set to a few degrees. The signal can be written

$$I(H,t) = I_0 \sin^2\left[\theta_\varepsilon + \Theta_{\mathrm{K}}(H,t)\right] \approx I_0\theta_\varepsilon + 2I_0\Theta_{\mathrm{K}}(H,t)\,,$$

where I_0 is the transmitted probe intensity and Θ_{K} is the Kerr rotation $\Theta_{\mathrm{K}} \ll \theta_\varepsilon$. The Kerr signal is superposed on a background, and the sensitivity of this method is therefore limited by the fluctuations of the laser. An improvement in the technique has been proposed that employ a polarization-sensitive balanced optical bridge, consisting of a Wollaston prism and a low noise differential detector [13]. In a high repetition rate laser system, the technique can be further improved via modulation of the polarization [63], which has the additional advantage of allowing simultaneous measurements of both the Kerr ellipticity and rotation. The Kerr configuration allows two types of measurements. The "magnetization" curve $M(H,t_0) \sim I(H,t_0) - I_0\theta_\varepsilon$ can be measured for a fixed pump-probe delay t_0 as a function of the magnetic field which is varied slowly. Alternatively, magnetization dynamics $M(H_0,t)$ can be measured for a fixed magnetic field H_0 as a function of the pump-probe delay t. In both cases, each data point corresponds to an average across ~1000 pulses.

The Nickel polycrystalline thin films have been evaporated on a glass substrate under high vacuum. The $\mathrm{CoPt_3}$ films consist of the alloy $\mathrm{Co_{0.25}Pt_{0.75}}$, grown at 690 K on a 16-nm Ru (0001) buffer layer deposited on a mica substrate. The growth conditions are chosen to optimize the perpendicular anisotropy [60]. A characterization of the magnetization as a function of temperature shows that magnetization at remanence vanishes at 635 K. The ferro-paramagnetic transition occurs in a broad temperature range, which can be explained by the chemical disorder in the alloy.

5.2.2 Time-Resolved Second-Harmonic Generation

Magnetic second-harmonic generation is another technique that has been used to measure magnetization dynamics on a femtosecond time-scale on Ni and Co surfaces [7,61]. In these experiments, the temporal resolution is also obtained with a pump-probe technique, but, instead of measuring the modifications induced by the pump on the probe, the intensity variations of the second-harmonic field signal by the probe are detected. Both the pump and the probe beams must have high flow (to have a measurable SHG yield). They are produced by a Ti:sapphire regenerative amplifier. Temporal resolutions down to 40 fs have been reported [62] with typical energy density of ~6 mJ cm^{-2} on the sample. In this type of experiment, the raw signal is the SHG intensity obtained with different orientations of a static magnetic field H parallel to the plane of the sample. Careful filtering of the fundamental component $I(\omega)$ is obtained with color filters and prism spatial dispersion. $I(2\omega)$ is measured with a photomultiplier, and the probe beam is chopped to perform phase-sensitive detection. Experimental results using these techniques are reported in the next section.

5.2.3 Spin-Resolved Photoemission

Spin-resolved photoemission is a well-known technique for studying electronic and magnetic properties of ferromagnets [64,65]. More recently, it has been used to study dynamic effects [2,8,9]. In such experiments, an intense pump pulse excites the sample, and electrons are photoexcited in vacuum using a time-delayed probe pulse having a shorter wavelength. Then, the spin polarization of the photoelectrons is measured by a spin detector (e.g., Mott detector). Because most metals have work functions in the range of 4–6 eV, UV laser pulses have to be used. This can be achieved, for instance, with the fourth harmonic of a titanium:sapphire. laser. The photoelectrons emitted by the sample have a short mean free path in metals (typically a few interatomic distances), so that the technique is very sensitive to the surface. This technique is powerful because it allows us to measure the spin polarization of the excited electrons directly in the energy-momentum space. However, it suffers from the very low efficiency of spin detection and also from experimental difficulties inherent in the detection of electrons in the presence of an applied magnetic field. Experimental results using these techniques are reported in the next section.

5.3 Experimental Studies:
Electrons and Spin Dynamics in Ferromagnets

In this section, we discuss experimental results concerning the ultrafast magnetization dynamics of Ni and CoPt$_3$ thin films.

5.3.1 Nickel Films

The spin dynamics in thin and ultrathin Ni films has been studied by several groups [6,7,8,63]. This material has the lowest Curie temperature among ferromagnetic transition-metal elements (631 K).

The first report of spin dynamics of a metallic ferromagnet on the femtosecond timescale was given by *Beaurepaire* et al. and can be found in [6]. Measurements were performed on a 22-nm thick Ni film deposited on optical glass and protected by a dielectric layer. The corresponding experimental conditions are described in detail in Sect. 5.2. In Fig. 14, the remanent Kerr signal $M_R(t)/M_0$ is reported as a function of pump-probe delay. M_R, which is obtained from the hysteresis loops measured at each delay t and normalized with the signal measured without pump beam M_0, drops by about 40% during the first picosecond. Its recovery time is much longer (several tens of picoseconds). To have more insight into magnetization dynamics, we compare in Fig. 15 the saturation MOKE signal $M_S(t)$ with the differential transmission signal during the first picosecond. In that case, $M_S(t)$ is measured in a static saturating magnetic field. $\Delta T/T$ reaches a maximum at $t \sim 250$ fs with a rise time limited only by the temporal resolution of 120 fs and then decreases. On the other hand, $M_S(t)$ continuously decreases on the entire temporal range displayed. The characteristic time of this demagnetization is $\tau_m \sim 200$ fs. It is obtained by a convolution of the pulse envelope with an exponential decay (*full line* in Fig. 15).

The magnetization dynamics of two Ni films 0.6 and 1.2 nm thick, deposited on a Ag(100) single crystal, was also studied by femtosecond time- and spin-resolved two-photon photoemission by *Scholl* et al. [8]. Two distinct magnetization dynamics were observed in this experiment: (i) the spin polarization of photoemitted electrons drops rapidly (< 300 fs) in agreement with

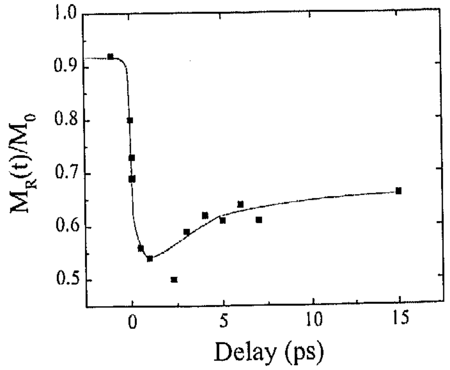

Fig. 14. Normalized Kerr signal at remanence for a 22-nm Ni film excited by 7 mJ/cm^2, 60 fs duration pump pulses. The solid line is a guide for the eyes

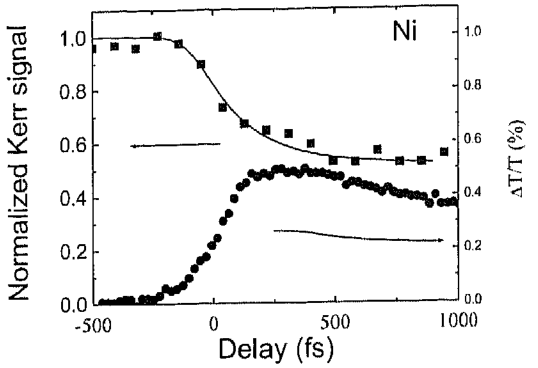

Fig. 15. Transient transmissivity $\Delta T/T(t)$ (*circles*) and MOKE signal (*squares*) of a 22-nm Ni film after excitation by 120-fs duration pump pulses at 800-nm wavelength. The *solid line* is a fit assuming an exponential decay of the magnetization ($\tau_{\mathrm{m}} = 200\,\mathrm{fs}$)

the previous MOKE experiment [6]; (ii) then a plateau occurs until $\sim 300\,\mathrm{ps}$ that is followed by a smoother magnetization decrease. The magnetization of a 0.6-nm film, which has a low Curie temperature $T_{\mathrm{c}} = 360\,\mathrm{K}$, vanishes at a delay of $\sim 800\,\mathrm{ps}$.

Hohlfeld et al. carried out pump and probe second-harmonic generation experiments. They considered both a polycrystalline bulk Ni/air interface [7] and epitaxial Ni ultrathin films (studied in ultrahigh vacuum) [61,62]. The measured quantity is the time and magnetization dependent SHG intensity $I(2\omega, M, t)$. The following normalized quantities can be defined:

$$\Delta I^{\pm}(t) = [I^{\pm}(t) - I_0^{\pm}]/I_0^{\pm} \tag{44}$$

with $I^{\pm} = I(2\omega, M, t) - I(2\omega, -M, t)$, where $I(2\omega, \pm M)$ are defined in (42). The 0 subscript corresponds to the signal measured in the absence of the pump beam. At the lowest order in M and with the definitions of Sect. 5.1, the following are relations between the second-order susceptibilities and the magnetization:

$$\chi^{(2)}_{\mathrm{odd}}(t, M) = \chi^{(2)}_{\mathrm{odd},0}(t)\, M(t)$$

and

$$\chi^{(2)}_{\mathrm{even}}(t, M) = \chi^{(2)}_{\mathrm{even},0}(t)\ .$$

This approximation leads to

$$\begin{aligned}\Delta I^{+} = {} & \frac{1}{\left|\chi^{(2)}_{\mathrm{odd},0}(0)\right|^2 M(0)^2 + \left|\chi^{(2)}_{\mathrm{even},0}(0)\right|^2} \\ & \times \left[\left|\chi^{(2)}_{\mathrm{odd},0}(t)\right|^2 M(t)^2 - \left|\chi^{(2)}_{\mathrm{odd},0}(0)\right|^2 M(0)^2 \right. \\ & \left. + \left|\chi^{(2)}_{\mathrm{even},0}(t)\right|^2 - \left|\chi^{(2)}_{\mathrm{even},0}(0)\right|^2 \right]\end{aligned} \tag{45}$$

and

$$\Delta I^{-} = \frac{\left|\chi^{(2)}_{\mathrm{even},0}(t)\right| \left|\chi^{(2)}_{\mathrm{odd},0}(t)\right| M(t) \cos[\phi(t)]}{\left|\chi^{(2)}_{\mathrm{even},0}(0)\right| \left|\chi^{(2)}_{\mathrm{odd},0}(0)\right| M(0) \cos[\phi(0)]} - 1\,. \tag{46}$$

With the further assumption that $\chi^{(2)}_{\mathrm{odd},0}(t)$ and $\chi^{(2)}_{\mathrm{even},0}(t)$ are time-independent and that the magnetization has a square root dependence on the electron temperature,

$$M(t) = M(T_0)\,\{1 - \mathrm{const}\,[T_{\mathrm{e}}(t) - T_0]\}^{1/2}\,. \tag{47}$$

Hohlfeld and co-workers [7] found experimentally that

$$\Delta I^{+} = \mathrm{const}[T_0 - T_{\mathrm{e}}(t)]\,, \tag{48a}$$

$$\Delta I^{-} = M[T_{\mathrm{e}}(t)]/M(T_0)\cos\phi - 1\,. \tag{48b}$$

With the assumptions above, the authors found a quadratic dependence of $1 + \Delta I^{-}$ versus ΔI^{+} for temporal delays $t > 300\,\mathrm{fs}$, which they interpret as a variation of magnetization with electron temperature, similar to the static curve *M(T)*. For a short time delay, the minimum in ΔI^{-} is reached earlier than in ΔI^{+}. This behavior is interpreted as a magnetic response faster than electron thermalization. As discussed in the following, this interpretation is misleading.

Later results obtained by the same group, using the same technique with a time resolution of 40 fs showed no detectable delays between magnetization and electron temperature [62]. In [62], the magnetic and electronic responses are associated with other quantities. Instead of using the definition (44), they used $S^{\pm} = [I(2\omega, M, t)]^{1/2} \pm [I(2\omega, -M, t)]^{1/2}$. Assuming $\left|\chi^{(2)}_{\mathrm{even},0}(t)\right| \gg \left|\chi^{(2)}_{\mathrm{odd},0}(t)\right| M(t)$, they found that $S^{+}(t)$ and $S^{-}(t)$ related, respectively, to electronic and magnetic dynamics.

Koopmans et al. measured spin dynamics from time-resolved MOKE experiments for buried Ni layers (thickness in the nanometer range) epitaxially grown on Cu(001) [63]. The system is interesting because an unusual spin reorientation, due to the strains induced by the lattice mismatch, takes place as a function of thickness. The easy magnetic axis is out of plane for a film thickness in the range from 1.2 to about 10 nm. The authors used a double modulation setup: the pump beam intensity is modulated by a mechanical chopper, and the probebeam polarization is modulated by a photoelastic device. This configuration allows one to measure the dynamics of both rotation and Kerr ellipticity. During the first 500 fs, the results show that these two quantities display different dynamics. Therefore, the authors concluded that there is no simple relationship between magneto-optical signals and magnetization on the subpicosecond timescale.

5.3.2 CoPt$_3$ Alloy Films

Co$_x$Pt$_{1-x}$ compounds possess enhanced magnetic properties due to the combination of the high exchange energy of Co and the high spin orbit energy of Pt. It was recently shown that CoPt$_3$ alloy films have large perpendicular magnetocrystalline anisotropy, large Kerr rotations at short wavelengths, and a Curie temperature close to room temperature [66]. These properties make them good candidates for high-density magneto-optical recording. The ultrafast spin dynamics of this system have been studied by two groups [10,13].

Ju et al. studied 20-nm (poly-)crystalline CoPt$_3$ films deposited on glass substrates, using optical pulses at 434 nm with a high repetition rate of 76 MHz [13]. They measured the differential reflectivities of the sample $\left[\frac{\Delta R}{R}(t)\right]_{\sigma\,\mathrm{pump},\sigma\,\mathrm{probe}}$ in four different combinations of pump and probe polarizations: $\sigma_{\mathrm{pump}} = \sigma^{\pm}$, $\sigma_{\mathrm{probe}} = \sigma^{\pm}$. The sample is placed in a static magnetic field. The transient Kerr ellipticity is given by

$$\Delta\varepsilon_{\mathrm{K},\sigma^{\pm}}(t) \approx \left[\frac{\Delta R}{R}(t)\right]_{\sigma^{\pm},\sigma^{+}} - \left[\frac{\Delta R}{R}(t)\right]_{\sigma^{\pm},\sigma^{-}} .$$

With a pump flow of ~ 1 µJ cm^{-2}, the authors observed that the measured transient Kerr ellipticity depends only on the pump polarization for the shortest time delay ($\leq$1 ps). From this, it was inferred that the response can be split into a thermalized spin population leading to a pump polarization-independent ellipticity change: $\Delta\varepsilon_{\mathrm{Kth}}(t) = \frac{1}{2}[\Delta\varepsilon_{\mathrm{K}\sigma^{+}}(t) + \Delta\varepsilon_{\mathrm{K}\sigma^{-}}(t)]$, and a nonthermal spin population: $\Delta\varepsilon_{\mathrm{Knonth}}(t) = \frac{1}{2}[\Delta\varepsilon_{\mathrm{K}\sigma^{+}}(t) - \Delta\varepsilon_{\mathrm{K}\sigma^{-}}(t)]$. The nonthermal contribution appears as a nearly symmetrical peak, with FWHM ~1 ps. On the other hand, the thermalized spin contribution has a rise time of 1.6 ps and a longer decay time (~10 ps).

Two authors of this review (E.B, J.-Y.B) studied epitaxial CoPt$_3$ films 48 nm thick under much higher pump flow (~ 10 mJ cm^{-2} at $\lambda = 800$ nm) using the experimental technique described in Fig. 13 [10]. Under these conditions, the magnetic hysteresis of the film disappears for a pump-probe time delay of about 630 fs, as shown in Fig. 16a. It shows that the film can be driven to the paramagnetic phase in such a short timescale. The dynamics of the polar MOKE signal, measured in an applied field of 1.7 kOe, is shown in Fig. 16b. It is similar to what was previously observed for Ni films (see Fig. 15). The nonvanishing signal measured at delays > 600 fs is explained by the polarization of the paramagnetic moments in the measuring field. From these data, the characteristic time for the ferro-paramagnetic phase transition is ~ 100 fs, that is comparable to the duration of the pulses used in the experiment (120 fs). The observed dynamics is also only weakly dependent on the polarization state (circular or linear) of the pump beam. This may suggest that the dominant mechanism of spin dynamics does not imply direct transfer of angular momentum from photons to spins.

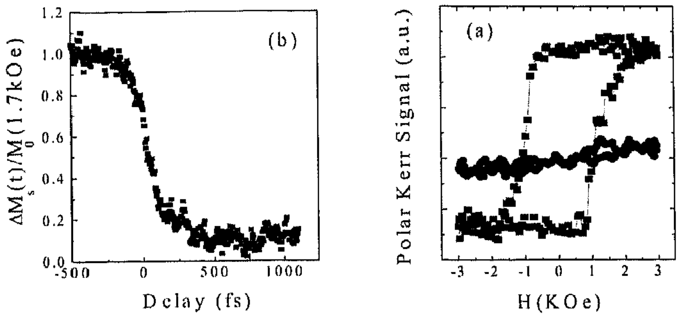

Fig. 16. Time-resolved polar MOKE results for a CoPt$_3$ film. (**a**) hysteresis loops measured without the pump beam (*square*) and for 630-fs pump-probe delay (*circle*). (**b**) MOKE dynamics measured in a static magnetic field (1.7 kOe)

6 Discussion

As reported in the preceding sections, experimental results obtained by different groups lead to various interpretations of spin dynamics. In this context, two main questions should be addressed: how accurate is the interpretation of a magneto-optic signal, obtained with a given technique, in terms of spin dynamics? How much is spin dynamics influenced by the particular sample which is studied? We will now discuss the different results with these two questions in mind.

To attribute the observed magneto-optical signals to a magnetization effect, it is important to study dynamics for different conditions of an applied magnetic field H. Even though ferromagnetic materials have spontaneous magnetization, this magnetization is sensitive to extrinsic parameters which lead to different magnetic domains and which may be altered after each pump pulse excitation. Therefore, it is important to restore the initial magnetic state of the sample between two laser pulses. Another advantage is that the symmetry of the pump-probe response can be checked under a reversed applied field $\pm H$. It is in this spirit that time-resolved magneto-optic Kerr experiments have been done with Ni and $\mathrm{CoPt_3}$ by the present authors [6,10]. In each case, the full magnetic hysteresis $M(H)$ was measured as a function of the pump-probe delay t. For $\mathrm{CoPt_3}$, the disappearance of hysteresis for $t > 500\,\mathrm{fs}$ can be unambiguously related to complete demagnetization of the sample, independently of the domain structure. Let us emphasize that it is the probe beam which is frequency modulated in these experiments, and not the pump, as in conventional transmission or reflectivity pump-probe experiments.

The magneto-optic SHG experiments, performed a with reversed applied field, also contain information on magnetization dynamics. However, different results have been obtained with the same technique but using a different temporal resolution. In a first experiment [7], magnetization dynamics preceded electron dynamics. In a later experiment [62] performed with 40-fs temporal resolution, no delay between $M(t)$ and electron dynamics was observed. In both cases, the magnetization response to the pump pulse is shorter than that observed in [6]. This discrepancy may be explained by two major differences in the techniques. First, with magneto-optic SHG, it is the surface of the sample which is mainly probed, whereas in the Kerr or Faraday pump-probe geometry, it is the bulk. The faster magnetization dynamics reported by *Hohlfeld* and co-workers may then be due to different behavior between magnetic states at the surface and in the bulk. Second, the interpretation of the SHG experiments in terms of separated electronic and magnetic contributions has to be taken cautiously. The expressions of $\Delta I^{\pm}(t)$ in (45) and (46) contain mixed electronic and magnetic terms. A first analysis of the SHG experiments [7] assumes two strong approximations: $\chi^{(2)}_{\mathrm{even},0}$ and $\chi^{(2)}_{\mathrm{odd},0}$ are independent of time, and electronic temperature $T_{\mathrm{e}}(t)$ has a parabolic dependence on magnetization. The first assumption is certainly not valid for small time delays. The second approximation is not consistent because substitution of (47) into (46) instead of (45) would lead to the opposite interpretation that the electronic response precedes the magnetic response. Another analysis of the SHG experiments [62] assumes the weaker approximation,

$$\left|\chi^{(2)}_{\mathrm{even}}(t)\right| \quad \gg \quad \left|\chi^{(2)}_{\mathrm{odd}}(t)\right| ,$$

to separate the electronic and magnetic contributions.

The work of *Koopmans* and co-workers [63] shows that, because the Kerr rotation and ellipticity have different dynamics in nickel, it is difficult to extract independent information on the magnetization and electronic contributions for small time delays. An additional difficulty arises from the contribution of a pump-induced Kerr rotation. Such a contribution is reported elsewhere in a study where we have stressed the effects of coherent pump-probe coupling, as well as optical orientation, which is not related to magnetization [67]. These remarks show that to determine magnetization dynamics, determining the ferromagnetic hysteresis loops $M(H,t)$ is a key measurement [6].

The photo emission experiments by *Scholl* and co-workers [8] focused on both the short and long time-delay behavior of magnetization. The initial subpicosecond demagnetization observed is consistent with the Kerr pump-probe results [6]. The authors attribute it to the excitation of Stoner pairs. This explanation is compatible with ultrafast demagnetization of the metal related to the initial hot electron distribution induced by the pump pulse [68].

The photoemission experiments on ultrathin films of nickel [8] also display a reduction of spin polarization on the timescale of 500 ps which is attributed to phonon–magnon scattering. This mechanism is consistent with the fact that the interaction of long wavelength spin-waves with the lattice is effective for long temporal delays. Similar observations have been reported recently for antiferromagnetic spin-waves in $\mathrm{Cr_2O_3}$ [69]. One should stress that the long timescale, which is necessary to obtain complete demagnetization of ultrathin Ni films, is not observed with the thicker films studied in [62]. This may be due to the low Curie temperature of the ultrathin films or to possible heat propagation effects in the metallic Cu substrate supporting the 1.2-nm thick Ni films.

Finally, let us come back to the problem of out-of-equilibrium dynamics of charges and spins. As mentioned above, it is now well recognized that femtosecond pulses excite nascent electron distributions which are not thermalized and that the corresponding thermalization time, due to electron–electron scattering, lasts a few hundreds of femtoseconds. One may wonder if non-equilibrium spin populations in this athermal regime could also be evidenced. An attempt to observe this regime was made in $\mathrm{CoPt_3}$ films [13]. The authors observed a peak in the signal $\Delta\varepsilon_{\mathrm{K\,nonth}}(t)$ which is interpreted as the manifestation of a coherent spin population relaxing with a time constant of $\sim 600\,\mathrm{fs}$. Such a “long” coherence time, however, disagrees with recent similar studies in nickel films performed without an applied magnetic field [70]. In these experiments, the coherent contribution lasts during a pulse excitation that is 40 fs. Both results raise the question of the distinction between electronic and spin coherence effects.

7 Conclusion

In conclusion, we reviewed experimental and theoretical results related to the ultrafast demagnetization, femtomagnetism, of ferromagnetic metallic thin films that can be induced with femtosecond optical pulses. In particular, we focused on the demagnetization dynamics observed in Ni [6,7,8,62,63] and $\mathrm{CoPt_3}$ thin films [10,13]. Until now, three experimental techniques with femtosecond resolution were used to address this topic: linear magneto-optics

(LMO), nonlinear magneto-optics (NLMO), and spin-resolved photoemission. Spin dynamics with characteristic timescales of ~100 fs have been observed. However, the interpretation of such dynamics in terms of magnetization dynamics, especially for short delays, has been controversial. Some convincing arguments suggest that indeed intrinsic demagnetization takes place on this timescale. First, complete demagnetization (i.e., vanishing MO signal) was observed within 500 fs or less in $\mathrm{CoPt_3}$ films using LMO [10] and in Ni ultrathin films using NLMO [61]. Secondly, similar dynamics have been observed by spin-resolved photoemission in Ni/Ag(100) films [8]; this technique may be viewed as a more direct probe of the magnetization of the surfaces. Nevertheless, this initial demagnetization dynamics takes place during the thermalization of the hot electron population. It was demonstrated that due to this effect, the MO observables and the sample magnetization are not proportional in this temporal regime [63].

A simple theory for the spin–lattice relaxation time τ_{sl} was outlined theoretically, on a longer timescale. It is found that τ_{sl} amounts to about 100 ps in typical ferromagnets, so that the experimentally observed spin dynamics takes place before energy transfer from the lattice to the spins. On a shorter timescale, to get a proper description of the ultimate processes, it is necessary to take into account the coupling between the spin polarized electronic system and the photon field. The first attempts in this direction were described. A time-dependent many-body Hamiltonian was solved with realistic parameters for a Ni monolayer. The excited system is prepared assuming a Gaussian energy distribution to mimic a short pulse, and the optical/MO observables are computed for each time step. It is found that the intrinsic theoretical limitation to spin and charge dynamics is of the order of 10 fs; spin dynamics is slightly slower. The phenomena are attributed to the dephasing of excited-state wave functions. Recently, we extended our theory by including the laser field. The primary results already show us a rich picture of demagnetization. In the future, the topics are ample from both the fundamental and technological points of view. Coherent control of demagnetization would be the next step, which may lead directly to an application of femtomagnetism as an ultrafast gating controlled by a laser. The selection of the materials should well balance the fast dephasing and the rapid recovery of magnetization. A good alloy consisting of ferromagnetic metals and semiconductors is an ideal option because each represents an extreme. This yields a maximal integration of ferromagnetic materials into the existing technology. Theory should provide useful understanding and a crucial guideline for optimizing the material.

References

1. M. H. Kryder: Magneto-optic recording technology, J. Appl. Phys. **57**, 3913 (1985)

2. A. Vaterlaus, T. Beutler, F. Meier: Spin-lattice relaxation time of ferromagnetic gadolinium determined with time-resolved spin-polarized photoemission, Phys. Rev. Lett. **67**, 3314 (1991)
3. L. Landau, E. Lifshitz: On the theory of the dispersion of magnetic permeability in ferromagnetic bodies, Physik Z. Sowjetunion **8**, 153 (1935)
4. W. Hübner, G. P. Zhang: Ultrafast spin dynamics in nickel, Phys. Rev. B **58**, R5920 (1998)
5. G. D. Mahan: *Many-Body Physics*, 2nd ed. (Plenum, New York 1990)
6. E. Beaurepaire, J. -C. Merle, A. Daunois, J. Y. Bigot: Ultrafast spin dynamics in ferromagnetic nickel, Phys. Rev. Lett. **76**, 4250 (1996)
7. J. Hohlfeld, E. Matthias, R. Knorren, K. H. Bennemann: Nonequilibrium magnetization dynamics of nickel, Phys. Rev. Lett. **78**, 4861 (1997); ibid. **79**, 960 (1997) (erratum)
8. A. Scholl, L. Baumgarten, W. Eberhardt: Ultrafast spin dynamics of ferromagnetic thin films observed by fs spin-resolved two-photon photoemission, Phys. Rev. Lett. **79**, 5146 (1997)
9. M. Aeschlimann, M. Bauer, S. Pawlik, W. Weber, R. Burgermeister, D. Oberli, H. C. Siegmann: Ultrafast spin-dependent electron dynamics in fcc Co, Phys. Rev. Lett. **79**, 5158 (1997)
10. E. Beaurepaire, M. Maret, V. Halte, J. -C. Merle, A. Daunois, J. Y. Bigot: Spin dynamics in $\mathrm{CoPt_3}$ alloy films: A magnetic phase transition in the femtosecond timescale, Phys. Rev. B **58**, 12134 (1998)
11. G. P. Zhang, W. Hübner: Femtosecond electron and spin dynamics probed by nonlinear optics, Appl. Phys. B **68**, 495 (1999); G. P. Zhang, W. Hübner: Femtosecond spin dynamics in the time domain, J. Appl. Phys. **85**, 5657 (1999)
12. W. Hübner, G. P. Zhang: Femtosecond spin dynamics probed by linear and nonlinear magneto-optics, J. Magn. Magn. Mater. **189**, 101 (1998)
13. G. Ju, A. Vertikov, A. V. Nurmikko, C. Canady, G. Xiao, R. F. C. Farrow, A. Cebollada: Ultrafast nonequilibrium spin dynamics in a ferromagnetic thin film, Phys. Rev. B **57**, R700 (1998)
14. W. Heisenberg: Z. Phys. **49**, 619 (1928)
15. T. Holstein, H. Primakoff: Field dependence of the intrinsic domain magnetization of a ferromagnet, Phys. Rev. **58**, 1098 (1940)
16. J. Hubbard: Proc. R. Soc. London A **276**, 238 (1963)
17. P. Fulde: *Electron Correlation in Molecules and Solids, 3rd ed.* (Springer, Berlin, Heidelberg 1995)
18. J. Wahle, N. Blümer, J. Schling, K. Held, D. Vollhardt: Microscopic conditions favoring itinerant ferromagnetism, cond-mat/9711242
19. E. C. Stoner: Collective electron ferromagnetism, Proc. R. Soc. London A **165**, 372 (1938); Collective electron ferromagnetism II. Energy and specific heat, ibid. A **169**, 339 (1939)
20. The infinitesimal magnetic field sets the quantization axis
21. R. Orbach: Proc. R. Soc. London A **264**, 458 (1961) and **264**, 485 (1961)
22. P. L. Scott, C. D. Jeffries: Spin-lattice relaxation in some rare-earth salts at helium temperatures, Phys. Rev. **127**, 32 (1962)
23. W. Hübner: Theory of nonlinear surface magneto-optics for ferromagnetic nickel: Effects of band structure and matrix elements, Phys. Rev. B **42**, 11553 (1990);
    A. Lessard, T. H. Moos, W. Hübner: Magnetocrystalline anisotropy energy of

transition-metal thin films: A nonperturbative theory, Phys. Rev. B **56**, 2594 (1997);
T. H. Moos, W. Hübner, K. H. Bennemann: Magnetocrystalline anisotropy of a transition metal monlayer: A non-perturbative theory, Solid State Commun. **98**, 639 (1996)

24. W. Hübner, L. M. Falicov: Theory of spin-polarized electron-capture spectroscopy in ferromagnetic nickel, Phys. Rev. B **47**, 8783 (1993); C. Moore: Atomic Energy Levels, Natl. Bur. Stand. (U.S.) (U.S. GPO, Washington, DC 1971)
25. H. Takayama, K. Bohnen, P. Fulde: Magnetic surface anisotropy of transition metals, Phys. Rev. B **14**, 2287 (1976)
26. Methods going beyond the present approximation may become rather impractical, especially when one is mainly interested in the excited states rather than only in the ground state. For example, for 1000 K-points, as typically used in our calculations, the dimension of the total Hilbert space would exceed 10^{1000}, which is intractable for present computational facilities
27. W. L. O'Brien, B. P. Tonner: Orbital and spin sum rules in X-ray magnetic circular dichroism, Phys. Rev. B **50**, 12672 (1994)
28. S. Hüfner, G. K. Wertheim, N. V. Smith, M. M. Traum: Solid State Commun. **11**, 323 (1972); C. Guillot, Y. Ballu, J. Paigné, J. Lecante, K. P. Jain, P. Thiry, R. Pinchaux, Y. P'etroff, L. M. Falicov: Resonant photoemission in nickel metal, Phys. Rev. Lett. **39**, 1632 (1977)
29. Obviously there is no clear exponential envelope visible on this fast timescale. Thus our definition seems to be an appropriate choice
30. The relaxation time refers to the *delay time* between the probe and pump pulses, which can be detected experimentally. The experimental time resolution can be as short as attoseconds, as experiments revealed recently
    H. Petek, A. P. Heberle, W. Nessler, H. Nagano, S. Kubota, S. Matsunami, N. Moriya, S. Ogawa: Optical phase control of coherent electron dynamics in metals, Phys. Rev. Lett. **79**, 4649 (1997);
    M. U. Wehner, M. H. Ulm, D. S. Chemla, M. Wegener: Coherent control of electron-LO-phonon scattering in Bulk GaAs, Phys. Rev. Lett. **80**, 1992 (1998)
    The process occurs in the real time domain and the average over "one period of the light" is not needed
31. N. I. Zheludev, P. J. Bennett, H. Loh, S. V. Popov, I. R. Shatwell, Y. P. Svirko, V. E. Gusev, V. F. Kamalov, E. V. Slobodchikov: Cubic optical nonlinearity of free electrons in bulk gold, Opt. Lett. **20**, 1368 (1995)
32. P. Kner, S. Bar-Ad, M. V. Marquezini, D. S. Chemla, W. Schäfer: Magnetically enhanced exciton-exciton correlations in semiconductors, Phys. Rev. Lett. **78**, 1319 (1997)
33. G. L. Eesley: Observation of nonequilibrium electron heating in copper, Phys. Rev. Lett. **51** , 2140 (1983)
34. H. E. Elsayed-Ali, T. B. Norris, M. A. Pessot, G. A. Mourou: Time-resolved observation of electron-phonon relaxation in copper, Phys. Rev. Lett. **58**, 1212 (1987)
35. R. W. Schoenlein, W. Z. Lin, J. G. Fujimoto, G. L. Eesley: Femtosecond studies of nonequilibrium electronic processes in metals, Phys. Rev. Lett. **58**, 1680 (1987)

36. S. D. Brorson, A. Kazeroonian, J. S. Moodera, D. W. Face, T. K. Cheng, E. P. Ippen, M. S. Dresselhaus, G. Dresselhaus: Femtosecond room-temperature measurement of the electron–phonon coupling constant gamma in metallic superconductors, Phys. Rev. Lett. **64**, 2172 (1990)
37. R. H. M. Groeneveld, R. Sprik, A. Lagendijk: Effect of a nonthermal electron distribution on the electron–phonon energy relaxation process in noble metals, Phys. Rev. B **45**, 5079 (1992)
38. W. S. Fann, R. Storz, H. W. K. Tom, J. Bokor: Direct measurement of nonequilibrium electron-energy distributions in subpicosecond laser-heated gold films, Phys. Rev. Lett. **68**, 2834 (1992)
39. T. Q. Qiu, C. L. Tien: Heat transfer mechanisms during short-pulse laser heating of metals, Int. J. Heat Mass Transfer **35**, 719 (1992)
40. C.-K. Sun, F. Vallée, L. H. Acioli, E. P. Ippen, J. G. Fujimoto: Femtosecond-tunable measurement of electron thermalization in gold, Phys. Rev. B **50**, 15337 (1994)
41. For a recent review on the electron dynamics in metals, see the whole issue of Chem. Phys. **251** (2000)
42. M. I. Kaganov, I. M. Lifshits, L. V. Tanatarov: Sov. Phys. JETP **4**, 173 (1957)
43. S. I. Anisimov, B. L. Kapeliovich, T. L. Perel'man: Electron emission from metal surfaces exposed to ultrashort laser pulse, Sov. Phys. JETP **39**, 375 (1974)
44. P. B. Allen: Theory of thermal relaxation of electrons in metals, Phys. Rev. Lett. **59**, 1460 (1987)
45. C. Suarez, W. E. Bron, T. Juhasz: Dynamics and transport of electronic carriers in thin gold films, Phys. Rev. Lett. **75**, 4536 (1995)
46. V. E. Gusev, O. B. Wright: Ultrafast nonequilibrium dynamics of electrons in metals, Phys. Rev. B **57**, 2878 (1998)
47. D. Pines, P. Nozières: The Theory of Quantum Liquids (Benjamin, New York 1966)
48. R. Rosei, D. W. Lynch: Thermomodulation spectra of Al, AU and Cu, Phys. Rev. B **5**, 3883 (1972)
49. N. W. Ashcroft, N. D. Mermin: Solid State Physics (Saunders College, Philadelphia 1976)
50. J.-Y. Bigot, E. Beaurepaire, A. Daunois, J.-C. Merle: in *Ultrafast Phenomena X*, Springer Ser. Chem. Phys. 62, P. F. Barbara, J. G. Fujimoto, W. H. Knox, W. Zinth (Eds.) (Springer, Berlin, Heidelberg 1996)
51. M. B. Agranat, S. I. Ashitkov, A. B. Granovskii, G. I. Rukman: Interaction of picosecond laser pulses with the electron, spin an phonon subsystems of nickel, Sov. Phys.-JETP **59**, 804 (1984)
52. A. Y. Elezzabi, M. R. Freeman, M. Johnson: Direct measurement of the conduction electron spin–lattice relaxation time T1 in Gold, Phys. Rev. Lett. **77**, 3220 (1996)
53. W. Voigt: *Magneto- und Electro-Optik*, (Teubner, Leipzig 1908)
54. P. M. Oppeneer, T. Maurer, J. Sticht, J. Kübler: Ab initio calculated magneto-optical Kerr effect of ferromagnetic metals: Fe and Ni, Phys. Rev. B **45**, 10924 (1992);
    P. M. Oppeneer, J. Sticht, T. Maurer, J. Kübler: Ab initio investigation of microscopic enhancement factors in tuning the magneto-optical Kerr effect, Z. Phys. B **88**, 309 (1992)

55. Q. Y. Jin, H. Regensburger, R. Vollmer, J. Kirschner: Periodic oscillations of the surface magnetization during the growth of Co films on Cu(001), Phys. Rev. Lett. **80**, 4056 (1998)
56. T. Rasing: Nonlinear magneto-optical probing of magnetic interfaces, Appl. Phys. B **68**, 477 (1999)
57. B. Koopmans, A. M. Janner, H. A. Wierenga, T. Rasing, G. A. Sawatzky, F. van der Woude: Separation of interface and bulk contributions in second-harmonic generation from magnetic and non-magnetic multilayers, Appl. Phys. A **60**, 103 (1995)
58. W. Hübner, K. H. Bennemann: Electronic theory for the nonlinear magneto-optical response of transition metals at surfaces and interfaces: Dependence of the Kerr rotation on the polarization and magnetic easy axis, Phys. Rev. B **52**, 13411 (1995)
59. V. V. Pavlov, G. Tessier, C. Malouin, P. Georges, A. Brun, D. Renard, P. Meyer, J. Ferré, P. Beauvillain: Observation of magneto-optical second-harmonic generation with surface plasmon excitation in ultrathin Au/Co/Au films, Appl. Phys. Lett. **75**, 190 (1999)
60. M. Maret, M.-C. Cadeville, R. Poinsot, A. Herr, E. Beaurepaire, C. Monier: Structural order related to the magnetic anisotropy in epitaxial (111) CoPt$_3$ alloy films, J. Magn. Magn. Mater. **166**, 45 (1997)
61. U. Conrad, J. Güdde, V. Jahnke, E. Matthias: Ultrafast electron and magnetization dynamics of thin Ni and Co films on Cu(001) observed by time-resolved SHG, Appl. Phys. B **68**, 511 (1999)
62. J. Hohlfeld, J. Güdde, U. Conrad, O. Duhr, G. Korn, E. Matthias: Ultrafast magnetization dynamics of nickel, Appl. Phys. B **68**, 505 (1999)
    J. Güdde, U. Conrad, V. Jähnke, J. Hohlfeld, E. Matthias: Magnetization dynamics of Ni and Co films on Cu(001) and of bulk nickel surfaces, Phys. Rev. B **59**, R6608 (1999)
63. B. Koopmans, M. van Kampen, J. T. Kohlhepp, W. J. M. de Jonge: Femtosecond spin dynamics of epitaxial Cu(111)/Ni/Cu wedges, J. Appl. Phys **87**, 5070 (2000)
    B. Koopmans, M. van Kampen, J. T. Kohlhepp, W. J. M. de Jonge: Ultrafast magneto-optics in nickel: Magnetism or optics? Phys. Rev. Lett. **85**, 844 (2000)
64. J. Kessler: *Polarized Electrons*, 2nd ed. (Springer Verlag, Berlin 1985)
65. M. Campagna, D. T. Pierce, F. Meier, K. Sattler, H. C. Siegmann: *Emission of Polarized Electrons in Solids in Advances in Electronics and Electron Physics*, Vol. 41 (Academic, London 1976) p. 113
66. C. J. Lin, G. L. Gorman: Evaporated CoPt alloy films with strong perpendicular magnetic anisotropy, Appl. Phys. Lett. **61**, 1600 (1992)
67. L. Guidoni, E. Beaurepaire, J.-Y. Bigot: Magnetization dynamics in the femtosecond time scale in ferromagnetic metals, in Quantum Electronics Laser Science Conference, OSA Technical Digest Series (Opt. Soc. Am., Washington, DC 2000) p. 160
68. K. H. Bennemann: Ultrafast spin dynamics of magnetic metals in a nonequilibrium state, Rev. Mex. Fis. **44**, 533 (1998)
69. J. S. Dodge, A. B. Schumacher, J.-Y. Bigot, D. S. Chemla, N. Ingle, M. R. Beasley: Time-resolved optical observation of spin-wave dynamics, Phys. Rev. Lett. **83**, 4650 (1999)
70. P. J. Bennett, V. Albanis, Yu. P. Svirko, N. I. Zheludev: Femtosecond cubic optical nonlinearity of thin nickel films, Opt. Lett. **24**, 1373 (1999)